

Numerical modeling of CO₂ fracturing by the phase field approach

Mostafa Mollaali^a, Vahid Ziae-Rad^b, Yongxing Shen^{a,*}

^a*University of Michigan – Shanghai Jiao Tong University Joint Institute, Shanghai Jiao Tong University, Shanghai, China*

^b*Faculty of Civil, Water and Environmental Engineering, Shahid Beheshti University, Tehran, Iran*

Abstract

We propose a phase field model to simulate CO₂ fracturing under an isothermal condition. We take advantage of the ability of the phase field approach in predicting fracture initiation and branching, and also to avoid tracking the fracture path. We model the CO₂ as a compressible fluid by modifying Darcy's law. In particular, we assume the permeability is correlated to the phase field value by an exponential function. The dependence of the CO₂ density as a function of the pressure is captured by the Span-Wagner equation of state. The computed breakdown pressure values show good agreement with analytical solutions and experimental results.

Keywords: CO₂ fracturing, CO₂ fluid flow, phase field

2010 MSC: 65K10

1. Introduction

Shale gas is the natural gas trapped within the shale, or mudstone reservoir,⁵ [the most common sedimentary rock](#). Shale is a fine-grained, sedimentary rock composed of clay minerals and silt-sized particles. The shale has low permeability so that it significantly inhibits the gas flow from the reservoir rocks to the production wells. As a result, the economic feasibility of shale gas development relies on the effective stimulation of the reservoirs [1]. Shale gas has become an energy source of increasing worldwide interest due to the two technologies that have become mature in industry: horizontal drilling and hydraulic fracturing ¹⁰ technique [2].

To date, water-based fluids are the most important fluids regularly used in the commercial shale gas due to their ready availability and low cost. But there are also some disadvantages to use water-based fluids, namely water shortage, contamination of underground water, and low fracturing performance. Also,

*Corresponding author

Email address: yongxing.shen@sjtu.edu.cn (Yongxing Shen)

15 hydraulic fracturing cannot avoid the clay swelling problem in shale [2]. Due to these problems, researchers actively investigate non-aqueous (see [3]) and non-fluid fracturing techniques such as explosive based method [4].

16 Carbon dioxide (CO_2) is one of the non-aqueous fracturing fluids that is considered to be used for fracturing. CO_2 as a fracturing fluid has been successfully applied to fracturing unconventional gas reservoirs decades ago [5]. Since the critical temperature of CO_2 is 31.1°C , once the pressure exceeds its critical pressure of 7.38 MPa, it will change to the supercritical state [6]. It can be injected down-hole either in liquid or supercritical state. The main benefits of CO_2 as a fracturing fluid include reducing consumption of water and water contamination, keeping clays (smectite and illite) stabilized, and preventing metal leaching and chemical interactions.

17 Brown [7] proposed CO_2 as a fracturing fluid and circulating fluid in geothermal energy extraction. Middleton *et al.* [8] investigated the potential of using CO_2 as a fracturing fluid for commercial scale of shale production. In the laboratory scale, Ishida *et al.* [9, 10] conducted fracturing experiments by using supercritical CO_2 . Also, some researchers investigated the effect of different fracturing fluids [11, 12].

18 There exist two general approaches for modeling fracture. One is discrete models for fracture where the geometrical discontinuity is modeled by modifying the geometry of intact structure [13, 14, 15, 16]. The other is smeared crack models where the discontinuity is distributed over a finite width, such as the phase field [17] and the gradient-enhanced damage methods [18]. In this approach, an additional unknown and a length scale are introduced.

19 Phase field modeling of fracture has gained popularity since the beginning of this century. The phase field model by Bourdin *et al.* [17] is essentially a regularization of the variational formulation of brittle fracture by Francfort and Marigo [19]. What makes the phase field an attractive approach can be attributed to its convenience in simulating complex fracture processes, including crack initiation, propagation, branching and merging. Compared to discrete fracture descriptions, the phase field approaches avoid tracking the complicated crack geometry; instead, the crack evolution is a natural outcome of the numerical solution to a constrained optimization problem. Thus, it significantly decreases the implementation difficulty, especially when dealing with 3D problems.

20 Bourdin *et al.* [20] have adopted the phase field approach to model hydraulic fracturing in impermeable media by considering the force that fluid pressure exerts on fracture surfaces. Afterwards, phase field approaches for hydraulic fracture in porous media based on Biot's equations and the theory of porous media have been investigated by many researchers.

21 Mikelić *et al.* [21] model pressurized fracture in porous media by combining the Biot theory and phase field approach. To minimize code modifications for adopting the phase field approach with an existing reservoir simulator, Yoshioka and Bourdin [22] have proposed an efficient framework by modifying the Darcy law. Wick *et al.* [23] have developed a model to simulate fluid-filled fracture propagation coupled to a reservoir simulator. Also, they have used a single pressure equation for the entire fractured domain by introducing a function to

distinguish between reservoir and fracture domains. Mauthe and Miehe [24] have coupled the phase field hydraulic fracture and porous media fluid flow by using a permeability decomposition. Ehlers and Luo [25] have combined the theory of porous media (TPM) and the phase field approach to fracture. Also, Culp *et al.* [26] have applied the phase field approach to fracture in CO₂ sequestration. In most cases researchers have supposed the fracturing fluid is incompressible or slightly compressible. Recently, Heider and Markert [27] proposed a method to model the pore fluid which is considered compressible.

The objective of the paper at hand is to propose a phase field model to investigate the effect of CO₂ as a compressible fracturing fluid under the isothermal condition, as the first step towards such modeling. For this purpose, we have adopted the phase field approach to model fracturing in porous media according to Mikelić *et al.* [21]. We model the CO₂ flow as a compressible fluid by modifying Darcy's law. We suppose permeability is correlated to the phase field value by an exponential function. The CO₂ density varies significantly with pressure, which is captured by the Span-Wagner equation of state [28].

In the remaining paper we will proceed as follows: a description of the fracture problem is given in Section 2, including the governing equations of the solid and the fluid flow. Afterwards, the numerical discretization and algorithm are constructed in Section 3. Then Section 4 provides numerical examples and discussions, where we will show that our results for the breakdown pressure agree well with not only widely used analytical solutions but also, within a reasonable error, with experimental results. Finally Section 5 draws conclusions.

2. Mathematical model

This section describes the mathematical model we will adopt for CO₂ fracturing. For convenience we will confine ourselves to the two-dimensional plane strain case, but the formulation is applicable to three dimensions with minimal changes. During the CO₂ fracturing process, the gas penetrates into the rock around the borehole and the injecting pressure causes the fracture to propagate. Thus, fracture propagation is a coupled phenomenon involving the gas flow inside the fracture and in the entire porous medium, the rock deformation, and the fracture propagation in the rock mass. In the following, in Section 2.1 we introduce the phase field method for fracture and derive the governing equations for the deformation and fracture propagation in the porous medium. Then, in Section 2.2 we present the governing equations for the gas flow within the porous medium. It is worth mentioning that compressible CO₂ exhibits a transport behavior different from that of slightly compressible fluids such as water and oil, due to its large compressibility and possibility of phase change.

2.1. Porous medium deformation and fracture propagation

In this section, we briefly recapitulate the basic notations and the underlying equations of the phase field method for pressurized fractures in brittle materials.

2.1.1. Variational formulation of brittle fracture

We consider a two-dimensional porous medium under plane strain loading occupying an open Lipschitz domain $\Omega \subset \mathbb{R}^2$. Let $\Gamma_D, \Gamma_N \subseteq \partial\Omega$ be such that $\Gamma_D \cup \Gamma_N = \partial\Omega$ and $\Gamma_D \cap \Gamma_N = \emptyset$, and $\mathbf{u}_D : \Gamma_D \rightarrow \mathbb{R}^2$ and $\mathbf{t}_N : \Gamma_N \rightarrow \mathbb{R}^2$ be prescribed displacement and traction boundary conditions, respectively. Also, let $\Gamma_B \subset \partial\Omega$ denote the boundary of a borehole. We let $Q_g : \Gamma_B \rightarrow \mathbb{R}$ denote the fluid source and $\mathbf{b} : \Omega \rightarrow \mathbb{R}^2$ the body force per unit volume exerted to the solid.

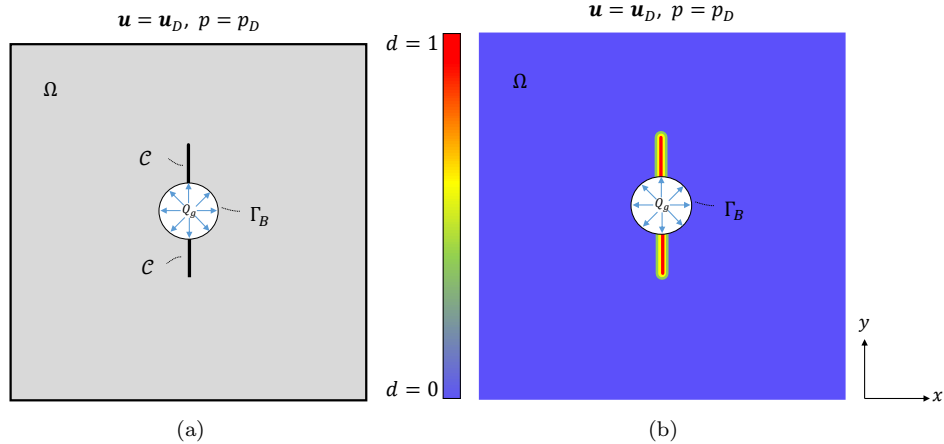


Figure 1: Schematic of (a) a sharp fracture and (b) the diffusive phase field profile for the same fracture. In both figures, a square plate with a borehole placed inside is shown. The *in situ* stress is applied on the external boundary, while the fluid is injected from the boundary of the borehole. We will only use the diffusive phase field in the proposed method.

The variational approach to fracture is built on energy minimization with respect to the displacement field $\mathbf{u} : \Omega \rightarrow \mathbb{R}^2$ and its jump set, which we denote as $\mathcal{C} = \mathcal{C}(\mathbf{u}) \subset \Omega$. Let $|\mathcal{C}|$ denote the one-dimensional Hausdorff measure of \mathcal{C} . Following Griffith's theory, the total potential energy of the fractured poroelastic solid is written as:

$$\begin{aligned} \Pi_{\mathcal{C}}[\mathbf{u}, \mathcal{C}] := & \int_{\Omega \setminus \mathcal{C}} \psi_0[\varepsilon(\mathbf{u})] \, d\Omega - \int_{\Omega} \mathbf{b} \cdot \mathbf{u} \, d\Omega - \int_{\Gamma_N} \mathbf{t}_N \cdot \mathbf{u} \, d\Gamma \\ & - \int_{\Omega \setminus \mathcal{C}} (\alpha - 1) p \operatorname{div} \mathbf{u} \, d\Omega + \int_{\Omega \setminus \mathcal{C}} \nabla p \cdot \mathbf{u} \, d\Omega + g_c |\mathcal{C}|, \end{aligned} \quad (1)$$

where p denotes the pore pressure, $\alpha \in [0, 1]$ is the Biot coefficient. Constant $g_c \in \mathbb{R}^+$ is the strain energy released per unit length of fracture extension. The strain energy density $\psi_0[\varepsilon(\mathbf{u})]$ is given by

$$\psi_0(\varepsilon) := \frac{\lambda}{2} (\operatorname{tr} \varepsilon)^2 + G \|\varepsilon\|^2,$$

with λ and G Lamé constants. These constants are related to Young's modulus E and Poisson's ratio ν as $\lambda = E\nu / [(1+\nu)(1-2\nu)]$ and $G = E / [2(1+\nu)]$. The

linearized strain tensor takes the form:

$$\boldsymbol{\varepsilon}(\mathbf{u}) := \frac{1}{2} (\nabla \mathbf{u} + \nabla \mathbf{u}^T).$$

¹¹⁰ Finally, $\|\cdot\|$ denotes the Frobenius norm of a tensor.

2.1.2. Regularized variational formulation of brittle fracture

To develop a numerical method to approximate (1), the phase field approach replaces the sharp-fracture description \mathcal{C} with a phase field description, where the phase field is denoted as $d : \Omega \rightarrow [0, 1]$. In particular, regions with $d = 0$ and $d = 1$ correspond to the intact and fully broken materials, respectively. Using a phase field approach, the one-dimensional fracture \mathcal{C} is approximated with the help of an elliptic functional [29, 30]:

$$\mathcal{C}_\ell[d] := \frac{1}{4c_w} \int_{\Omega} \left(\frac{w(d)}{\ell} + \ell \nabla d \cdot \nabla d \right) d\Omega, \quad (2)$$

where $\ell > 0$ is the regularization length scale, which may also be interpreted as a material property, e.g., the size of the process zone. See Remark 3 for comments on the choice of ℓ . Constant $c_w = \int_0^1 \sqrt{w(d)}$ is a normalization constant such that when $\ell \rightarrow 0$, $\mathcal{C}_\ell[d]$ converges to the length of the sharp fracture, $|\mathcal{C}|$. Classical examples of $w(d)$ and c_w are $w(d) = d^2$ and $c_w = 1/2$ for the AT2 model, and $w(d) = d$ and $c_w = 2/3$ for the AT1 model. Between these models, the AT1 model which is better at simulating crack nucleation [31] predicts a phase field profile with a support of a finite width, but requires solving inequality constrained optimization problems; the AT2 model, which normally requires a pre-existing crack (at least for a homogeneous material under low-speed loading), gives a diffuse phase field profile, but can be implemented as constrained optimization problems which are much easier to solve. Interested readers are referred to [31, 32] for more elaborations. In this paper all numerical examples are implemented with the AT1 model, while we keep our formulation general for both models.

On this basis, we replace (1) by a global constitutive dissipation functional for a rate independent fracture process [33]:

$$\begin{aligned} \Pi[\mathbf{u}, d] := & \int_{\Omega} \psi[\boldsymbol{\varepsilon}(\mathbf{u}), d] d\Omega - \int_{\Omega} \mathbf{b} \cdot \mathbf{u} d\Omega - \int_{\Gamma_N} \mathbf{t}_N \cdot \mathbf{u} d\Gamma \\ & - \int_{\Omega} (1-d)^2 (\alpha-1) p \operatorname{div} \mathbf{u} d\Omega + \int_{\Omega} (1-d)^2 \nabla p \cdot \mathbf{u} d\Omega \\ & + \frac{g_c}{4c_w} \int_{\Omega} \left(\frac{w(d)}{\ell} + \ell \nabla d \cdot \nabla d \right) d\Omega, \end{aligned} \quad (3)$$

where the admissible sets of displacement and phase field can be set as:

$$\mathcal{S}_u := \{ \mathbf{u} \in H^1(\Omega; \mathbb{R}^2) | \mathbf{u} = \mathbf{u}_D \text{ on } \Gamma_D \}, \quad (4a)$$

$$\mathcal{S}_d := \{ d \in H^1(\Omega) | 0 \leq d \leq 1 \}. \quad (4b)$$

In practice, (4b) will be used in combination with the irreversibility constraint, to be elaborated in Remark 2.

Remark 1 (Strain energy degradation). *The solid endures partial loss of stiffness due to the presence of fractures. In order to model this effect, the strain energy density is degraded with respect to the evolution of the phase field. Also note that as the damaged material responds differently to tension and compression, we let only a part of the strain energy density be degraded. For this purpose, we let the degraded strain energy in (3) take the following general form:*

$$\psi(\boldsymbol{\varepsilon}, d) = g(d)\psi_+ + \psi_-,$$

where $g(d)$ satisfies $g(0) = 1$, $g(1) = 0$, and $g'(d) < 0$ for all d such that $0 \leq d \leq 1$ [17]. A usual choice is $g(d) = (1-d)^2$. On the other hand, ψ_{\pm} are such that

$$\psi_+(\boldsymbol{\varepsilon}) + \psi_-(\boldsymbol{\varepsilon}) = \psi_0(\boldsymbol{\varepsilon}).$$

Now since $\partial\psi/\partial d = g'(d)\psi_+$, only ψ_+ contributes to fracture propagation.

There are several phase field models that differ in their choice of ψ_{\pm} . In this paper, we adopt the one proposed by Amor *et al.* [34]. This model assumes both volumetric expansion and deviatoric deformation contribute to fracture propagation, but volumetric compression does not. A decomposition of $\boldsymbol{\varepsilon}$ into volumetric and deviatoric parts reads:

$$\text{vol } \boldsymbol{\varepsilon} := \frac{1}{3}(\text{tr } \boldsymbol{\varepsilon})\mathbf{1}, \quad \text{dev } \boldsymbol{\varepsilon} := \boldsymbol{\varepsilon} - \text{vol } \boldsymbol{\varepsilon}.$$

¹³⁰ See AppendixA.1 for more details.

Remark 2 (Irreversibility constraint). *The requirement $g'(d) < 0$ comes from the underlying irreversibility condition (the fracture can never heal) in time:*

$$\partial_t d \geq 0. \tag{5}$$

Consequently, modeling of fracture evolution problems leads to inequality constraints, and sometimes gives rise to a variational inequality formulation.

¹³⁵ As an alternative way to model the irreversibility, Miehe *et al.* [35] proposed a phase field model based on a local history field. In this model, the evolution of the phase field d is driven by the historically maximum value of ψ_+ at the point of interest.

Remark 3 (The choice of ℓ). *Based on an analytical solution for the critical tensile strength σ_{cr} that a one-dimensional bar can sustain [32], we use the following equation for the choice of ℓ :*

$$\ell = \frac{3Eg_c}{8\sigma_{cr}^2}, \tag{6}$$

¹⁴⁰ where E and g_c can be obtained from regular experiments, while σ_{cr} can be approximated by the tensile strength σ_t . Assuming all other parameters are known, the formula (6) is able to estimate ℓ , though the accuracy is unknown for more complex cases.

2.2. Carbon dioxide as a compressible fluid

The governing equations for the fluid flow in a porous medium are given by mass conservation, momentum balance, and the equation of state. The mass conservation equation reads:

$$\begin{aligned} \partial_t(\phi\rho) + \nabla \cdot (\rho\mathbf{v}) &= 0 && \text{in } \Omega, \\ -\rho\mathbf{v} \cdot \mathbf{n} &= Q_g && \text{on } \Gamma_B. \end{aligned} \quad (7)$$

Here ϕ denotes the porosity of the porous medium (the fraction of volume occupied by the fluid), ρ the density of the fluid, \mathbf{v} the Darcy velocity vector, and Q_g the fluid source. Note that Q_g has the unit of volumetric flow rate per unit volume. Also, we assume the rock is saturated by the fluid so that the fluid content in rock per volume is expressed by $\phi\rho$.
145

In addition to (7), we state the momentum balance in the form of Darcy's law. Note that this assumption is for the flow in conventional reservoirs, although there are more complicated flow regimes, namely slip flow, transition flow, and Knudsen diffusion, for which Darcy's law in its current form cannot be used. For more details we refer the reader to [36, 37, 38, 39]. Nevertheless modeling the flow at the microscale is out of the scope of this paper that deals with a continuum formulation, and hence we confine ourselves to Darcy's law throughout this work. This implies a linear relationship between the fluid velocity and the head pressure gradient:

$$\mathbf{v} = -\frac{k}{\mu}\nabla p, \quad (8)$$

where $k = k(d)$ is the permeability of the rock, and μ is the dynamic fluid viscosity. Note that there could be an additional term $-\rho g \nabla z$ on the right hand side of (8), where g and z are the magnitude of the gravitational acceleration and the depth, respectively. This term is, however, in our case negligible, as we assume an almost horizontal computational domain. Also, we assume the porosity is not dependent on the stress condition.
150

On the other hand, we correlate the permeability to the phase field value as it is clear that when the crack starts propagating, the permeability of the solid matrix starts to increase, as the crack width increases. To incorporate this effect into our model, an exponential variation of the fluid permeability has been adopted from [40, 41]:

$$k(d) = k_0 \exp(\alpha_k d), \quad (9)$$

where k_0 is the permeability of the intact material, and α_k is a coefficient to indicate the effect of phase field evolution on the permeability. We take $\alpha_k = 7.0$ according to [41]. In real applications, α_k can be obtained from experiments. Figure 2 illustrates the permeability increasing with respect to the evolution of the phase field variable. As seen therein, the permeability starts from an initial value for a completely intact porous medium to a very big value of permeability in the fully broken area.
155

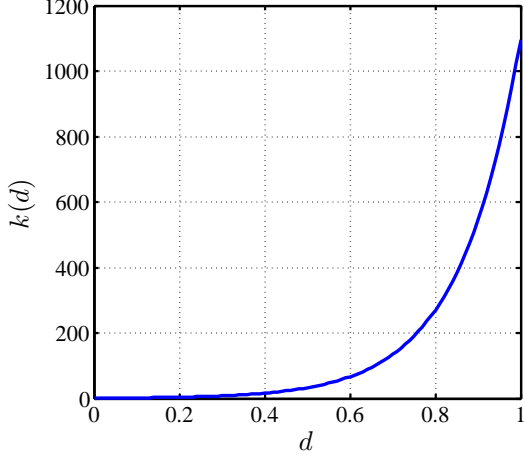


Figure 2: Plot of $k(d) = \exp(7.0d)$, permeability, as a function of the phase field variable d .

The first term on the left hand side of (7), the rate of change of fluid content, can be written as:

$$\partial_t(\phi\rho) = \rho \partial_t\phi + \phi \partial_t\rho = \rho \partial_t\varepsilon_v + \phi \partial_t\rho, \quad (10)$$

where we have assumed the rate of change of pore volume is equal to that of the volumetric strain, which is given by $\varepsilon_v = \nabla \cdot \mathbf{u}$.

Under isothermal conditions, the gas density varies significantly with pressure. This is captured by an equation of state (EOS). One applicable EOS for CO₂ is known as the Span-Wagner (S-W) equation [28] defined in terms of the Helmholtz free energy. The CO₂ density and pressure are related by:

$$p = (1 + \delta\varphi_\delta^r) \rho RT, \quad (11)$$

where R is the universal gas constant, and φ_δ^r is the derivative of the residual part of the full expression of Helmholtz energy φ^r with respect to the reduced density δ , with

$$\begin{aligned} \varphi^r(\delta, \tau) = & \sum_{i=1}^7 n_i \delta^{d_i} \tau^{t_i} + \sum_{i=8}^{34} n_i \delta^{d_i} \tau^{t_i} e^{-\delta^{c_i}} + \sum_{i=35}^{39} n_i \delta^{d_i} \tau^{t_i} e^{-\alpha_i(\delta-\varepsilon_i)^2 - \beta_i(\tau-\gamma_i)^2} \\ & + \sum_{i=40}^{42} n_i \Delta^{b_i} \delta e^{C_i(\delta-1)^2 - D_i(\tau-1)^2}, \end{aligned} \quad (12)$$

in which

$$\Delta = \left\{ (1 - \tau) + A_i \left[(\delta - 1)^2 \right] \frac{1}{2\beta_i} \right\}^2 + B_i \left[(\delta - 1)^2 \right]^{a_i}.$$

In (12), ρ_c and T_c are the critical density and temperature, respectively, and $\delta = \rho/\rho_c$ and $\tau = T/T_c$ are the reduced ones. For the sake of brevity, here we do not provide the definitions and values of other parameters in (12), but refer the readers to [28].

By substituting (8),(9), (10), and (11) in (7), the governing equation for CO₂ flow is written as follows:

$$\begin{aligned} \phi \partial_t \rho + \rho \partial_t \varepsilon_v - \nabla \cdot \left(\rho \frac{k(d)}{\mu} \nabla p \right) &= 0, \quad \text{in } \Omega, \\ \rho \mathbf{v} \cdot \mathbf{n} &= -Q_g, \quad \text{on } \Gamma_B, \\ p &= p_D, \quad \text{on } \Gamma_P, \end{aligned} \tag{13}$$

where $\Gamma_P = \partial\Omega \setminus \Gamma_B$.

Summary of governing equations. The governing equations for modeling the CO₂ fracturing are summarized as follow: for the porous medium deformation, the functional defined in (3) is minimized among $(\mathbf{u}, d) \in \mathcal{S}_u \times \mathcal{S}_d$ under the constraint (5), while for the compressible fluid the boundary value problem (13) is used to solve for the pressure p .

Advantages and limitations of the method. The main advantage of the current approach is its convenience in simulating complex fracture processes, including crack initiation, propagation and merging. In fact, the evolution of fracture surfaces is the natural outcome of the solution of a coupled system of partial differential equations. Such a model significantly decreases the implementation difficulty by avoiding tracking the fracture geometry. In this work, taking advantage of the phase field approach, we consider CO₂ as a compressible fracturing fluid under an isothermal condition. Nevertheless, as this work is the first of its kind, herein a relatively simple model is used for the calculation of gas flow and permeability in shale media.

3. Numerical solution

In this section we present an algorithm that adopts standard procedures to obtain a numerical method to solve the initial boundary value problem presented in Section 2. In this algorithm, a staggered approach is employed to solve the underlying equations, i.e., the solution is obtained via iteration between the variables [17, 42]. This idea is based on the fact that by fixing two variables, the problem becomes convex in the remaining unknown. However, one drawback for such an approach is that it might need many iterations to achieve convergence among the three fields.

For the problem at hand, we need to solve a coupled system consisting of mass balance for the compressible fluid and a dissipative potential energy with the phase field. We provide a fully iterative approach in which at each stage we solve for one unknown while the other two variables are fixed to their values at the last iteration. Readers are referred to Algorithm 1 for complete elaboration.

Algorithm 1: Algorithm for modeling the CO₂ by phase field.

Input: $p_0, d_0, \mathbf{u}_0, \rho_0$, and ε_{tol}
Output: p_n, d_n , and $\mathbf{u}_n, n = 1, \dots, N$

1 Set flow and mechanical boundary conditions σ_1, σ_3 , and Q_g ;
2 **for** $n = 1$ to N ; **do**

3 Set $t = n\Delta t$ and $k = 0$; /* k is an iteration counter */
4 **repeat**

5 $m = 0$; /* m is another iteration counter */
6 **repeat**

7 Step - P: compute p_n with (A.6);
8 Step - U: compute \mathbf{u}_n with (A.1);
9 Update $\rho_n^{(k+1)} \leftarrow \rho(p_n^{(k)})$ with (11);
10 $k + 1 \leftarrow k$

11 **until** $\|p_n^{(k)} - p_n^{(k-1)}\|_2 < \varepsilon_{\text{tol}}$ **and** $\|\mathbf{u}_n^{(k)} - \mathbf{u}_n^{(k-1)}\|_2 < \varepsilon_{\text{tol}}$;

12 Step - d: compute d_n with (A.1);
13 $m + 1 \leftarrow m$

14 **until** $\varepsilon_d = \|d_n^{(m)} - d_n^{(m-1)}\|_2 < \varepsilon_{\text{tol}}$;

15 $\mathbf{u}_{n-1} \leftarrow \mathbf{u}_n$;
16 $p_{n-1} \leftarrow p_n$;
17 $\rho_{n-1} \leftarrow \rho_n$;

18 **end**

We implement our method on FEniCS, an open-source finite element software [43, pp. 173–225]. Therein, the user merely needs to provide the variational form of the problem as well as the geometry and mesh information. Then, a big advantage of FEniCS is that the software itself completes all steps toward generating the global stiffness matrix.

Below we show an excerpt of the used FEniCS code. This piece of code performs some calculations for line 8 in Algorithm 1 wherein \mathbf{u} is solved for while the other two unknowns are fixed. It first defines $\boldsymbol{\varepsilon}$, ψ_0 , and $\psi(\boldsymbol{\varepsilon}, d)$ in lines 1, 3, and 5, respectively. Then, the standard finite element shape functions are defined in line 8, and the admissible function space (`TrialFunction`), the test function space (`TestFunction`), and the unknown function \mathbf{u} (`Function`) are defined in line 9. Afterwards, the elastic energy is introduced as a variational form in line 11. Finally, in lines 12 and 13, the code takes the first variation $\delta\Pi[(\mathbf{u}, d); \bar{\mathbf{u}}]$ (A.1a) and the second variation $\delta^2\Pi[(\mathbf{u}, d); \bar{\mathbf{u}}; \delta\mathbf{u}]$ (A.2a) and builds the nodal residual vector as `Residual_u` and the tangent stiffness matrix as `Jacobian_u`.

```

1 def eps(u_):
2     return sym(grad(u_))
215 def psi_0(u_):
4     return 0.5 * lmbda * tr(eps(u_))**2 + mu * eps(u_)**2
5 def psi_(u_, d_):
6     return ((1 - d_)**2 + k_ell) * psi_0(u_)
7
220 V_u = VectorFunctionSpace(mesh, "CG", 1)
9 u_, u, u_t = Function(V_u), TrialFunction(V_u), TestFunction(V_u)
10
11 energy_elastic = psi_(u_, d_) * dx
12 Residual_u = derivative(energy_elastic, u, u_t)
225 Jacobian_u = derivative(Residual, u_, u_t)

```

To solve the three unknowns, we select for \mathbf{u} and p the linear solver MUMPS which is convenient for solving large linear systems [44], and for d the TAO optimization solver integrated into the PETSc library [45, 46], which has the capability of solving inequality constrained optimization problems as the one at hand. Interested readers are referred to [47] for more information about the applied solvers.

4. Numerical examples

In this section, we present a set of numerical examples to demonstrate the capability of the proposed model. First, we aim to verify our implementation of the present phase field method for CO₂ fracturing. To this end, we present three examples with exact or otherwise well-established solutions to verify our outputs. Next, we present three more numerical example to demonstrate the capability of the proposed model.

²⁴⁰ We also refer the interested readers to Wilson and Landis [48] and Chukwudzie [49] in which the phase field approach to hydraulic fracturing is verified with classical two-dimensional analytical solutions [50, 51].

4.1. Single-edge-notched tension test

²⁴⁵ First, following an example motivated by Miehe *et al.* [52], we ^{first} investigate a square plate with a horizontal initial crack at the middle height starting from the left end and ending at the plate center. The geometric setup is depicted in Figure 10. To capture the crack pattern properly, the mesh is refined in areas where the crack is expected to propagate, i.e., in the center strip of the specimen. In effect, for a discretization with 105,352 standard P_1 elements, ²⁵⁰ an effective element size of $h \approx 5 \times 10^{-3}$ mm is obtained in the critical zone. The specimen is under a direct tension test, in which a monotonically increasing displacement with constant increments $\Delta\mathbf{u} = 6 \times 10^{-5}$ mm is imposed on the top edge while the bottom edge is fixed. In this example, the evolution is simulated for 100 uniform time steps so that a final deformation of 6×10^{-3} mm is reached. ²⁵⁵ We will adopt the values of the material parameters given in Table 1. Note that all our models are implemented with the AT1 model.

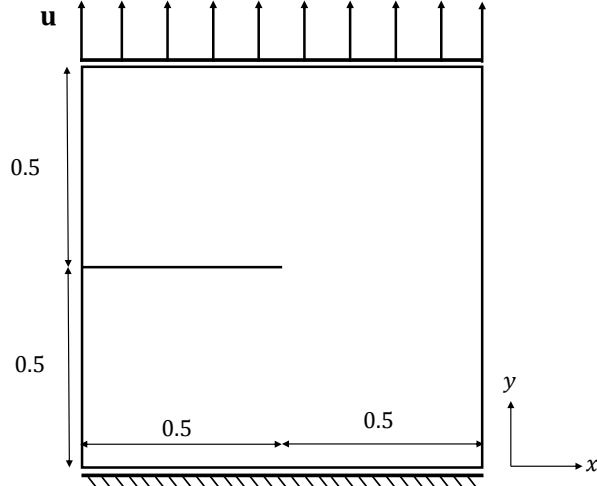


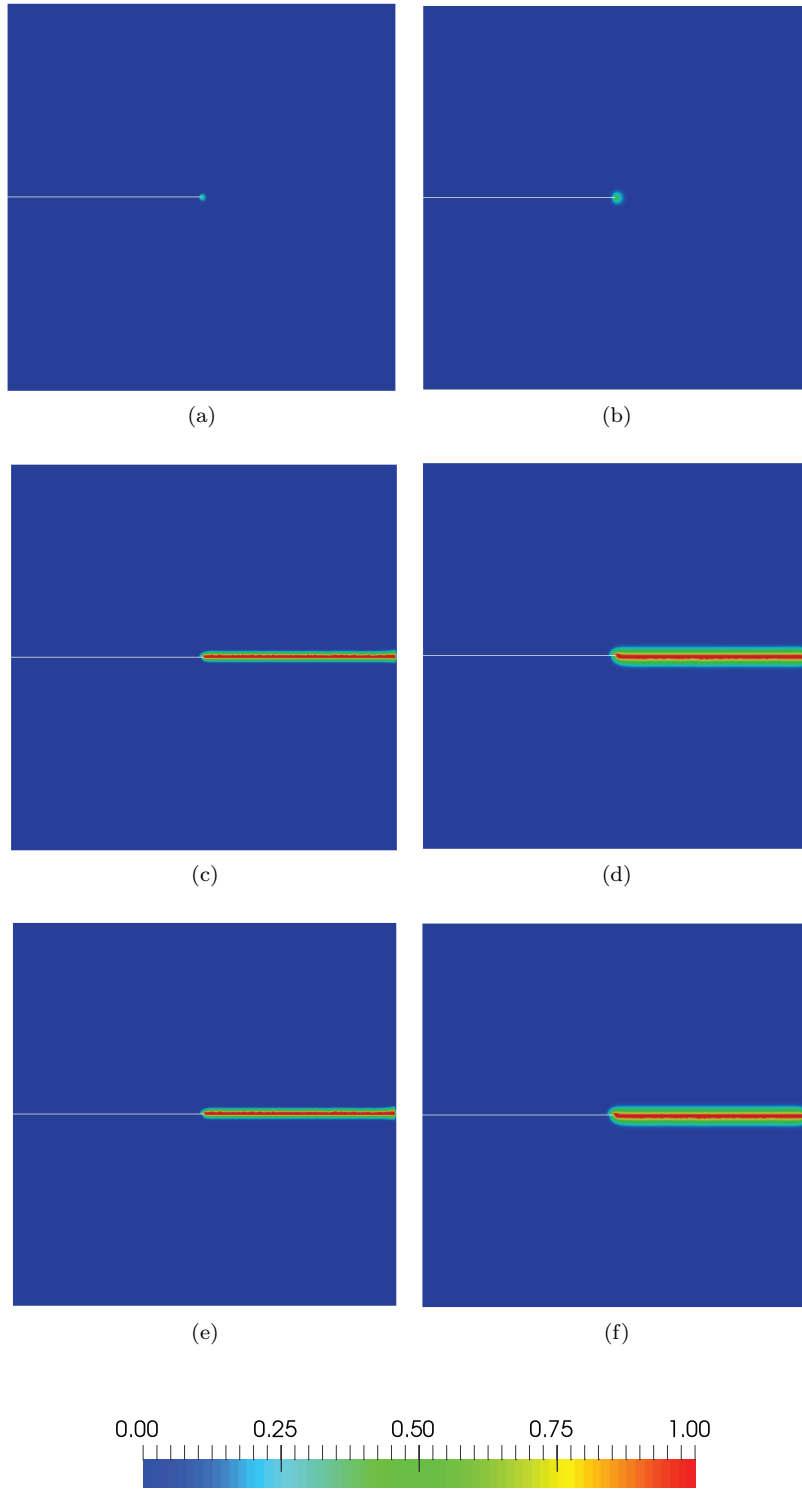
Figure 3: Schematic of a cracked square plate (unit: mm) under a single-edge-notched tension test. A monotonically increasing displacement with constant increments $\Delta\mathbf{u} = 6 \times 10^{-5}$ mm is applied on the top edge while the bottom edge is fixed.

Table 1: Cracked square plate under a tension test: Material parameters [53]

Parameters	symbol	unit	value
Young's modulus	E	MPa	210×10^3
Poisson's ratio	ν	—	0.3
Critical energy release rate	g_c	MPa·mm	2.7

The resulting crack patterns at different stages of the deformation for two fixed regularization length scales $\ell = \ell_1 = 1 \times 10^{-2}$ mm and $\ell = \ell_2 = 2 \times 10^{-2}$ mm are illustrated in Figure 4. As expected, in both simulations, the fracture propagates straightforward to the end. This straight crack topology agrees well with the results in [54]. Also as seen, the resulting crack pattern with the smaller ℓ looks sharper.

We also output the load-deflection curves for the two setups of Figure 5. As seen, both models will result in similar trends. Hence, the effect of ℓ on the response is small in this range.



14

Figure 4: Cracked square plate under a tension test with two different regularization length scales $\ell = \ell_1 = 10^{-2}$ mm $\approx 2h$ (left) and $\ell = \ell_2 = 2 \times 10^{-2}$ mm $\approx 4h$ (right). Both simulations are done with 100 uniform time steps with $\Delta u = 6 \times 10^{-5}$ mm (See also Table 1 for the input values). Phase field contours at three different stages $u = 5.52 \times 10^{-3}$ mm (4a,4b), $u = 5.58 \times 10^{-3}$ mm (4c,4d), and $u = 6 \times 10^{-3}$ mm (4e,4f) are shown in deformed configurations with the deformations scaled. The initial cracks are explicitly imposed, so in the deformed configuration it appears as a white line. As expected, we observe a straight crack pattern in both cases.

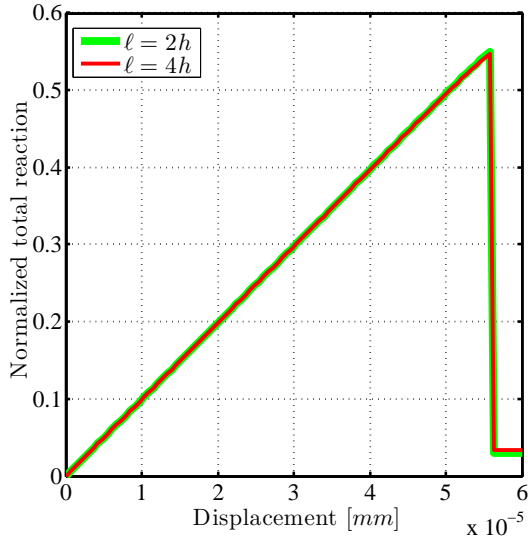


Figure 5: Cracked square plate under a tension test with two different regularization length scales $\ell = \ell_1 = 10^{-2}$ mm $\approx 2h$ (red) and $\ell = \ell_2 = 2 \times 10^{-2}$ mm $\approx 4h$ (green). Load-deflection curves for both ℓ_1 and ℓ_2 are obtained. Both simulations are done with 100 load steps with $\Delta u = 6 \times 10^{-5}$ mm. The total reaction is normalized by the one in the case without any crack or phase field evolution. Both models give rise to similar trends so the effect of changes in ℓ is small within this range. Note that the reaction highly decreases at the 93rd time step where the crack starts to propagate.

4.2. Poroelastic response of a borehole

This example aims to study the effect of fluid pressurization on the poroelastic response around the borehole. It was first studied by Detourneau and Cheng [55] (see also [11, 56]). Consider a plane strain hydraulic fracturing problem where there is a square plate containing a central borehole. The geometry and the loading conditions in this example are the same as Figure 12. The far-field *in situ* stress is set to zero in this example. Note also that $d \equiv 0$, i.e., there is no preexisting crack in the specimen and we do not allow for any nucleation of the fracture as the rock strength is assigned a very large value. A discretization with 28,140 standard P_1 elements is applied to the problem. To capture the high gradient of pressure near the borehole, the mesh is refined in that area so that an effective mesh size of $h \approx 0.15$ mm is adopted. The fluid is slightly compressible, and we set the fluid pressure in the borehole to 1 MPa. The other material properties are prescribed according to Table 2.

Here, the governing equation for the slightly compressible flow is written as follows [55]:

$$\partial_t p + M \nabla \cdot \left(\frac{k_0}{\mu} \nabla p \right) = 0$$

where $M = E(1-\nu)/[(1+\nu)(1-2\nu)]$ is called the constrained modulus.

Table 2: Poroelastic response of a borehole: Material parameters

Parameters	symbol	unit	value
Young's modulus	E	MPa	6000
Poisson's ratio	ν	—	0.34
Biot coefficient	α	—	1.
Permeability	k_0	mm^2	1×10^{-12}

Figure 6 shows the distribution of pore pressure around the borehole for three values of dynamic viscosity μ at early time $t = 0.1$ s. Note that the horizontal axis is $(r - r_0)/r_0$, ranging from 0 to 0.25 in the direction of $\theta = \pi/2$. The simulation results are then compared to the analytical solution by Detourneau and Cheng [55].

Figure 7 depicts the effect of dynamic viscosity on the effective tangential stress in the vicinity of the borehole at early time $t = 0.1$ s.

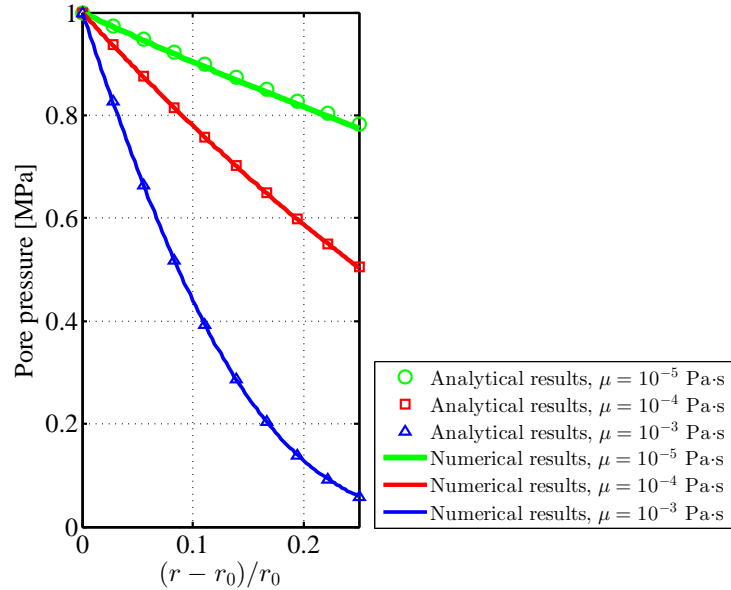


Figure 6: Poroelastic response of a borehole. The distribution of pore pressure caused by fluid pressurization is shown around the borehole for three different dynamic viscosities μ at early time $t = 0.1$ s. As seen, the results are in good accordance with the analytical in [55].

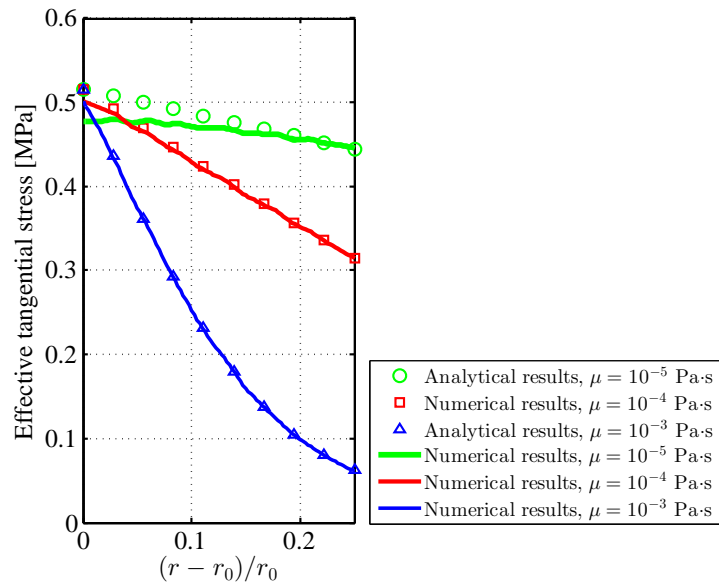


Figure 7: Poroelastic response of a borehole. The effective tangential stress is plotted near the borehole for three different dynamic viscosities μ at early time $t = 0.1$ s.

4.3. Computation of the crack opening displacement

We now focus on a classical problem first solved by Sneddon and Lowengrub [57] (see also [20]) that solves the opening displacement of a static line crack.

Consider a computational domain of $\Omega = 4 \text{ m} \times 4 \text{ m}$ with a preexisting line fracture of length $2a_0 = 0.4 \text{ m}$, i.e., $\mathcal{C} = [1.8, 2.2] \times \{0\}$. To minimize the effect of the boundary conditions on the results, the domain size is much larger than the crack length ($L \gg 2a_0$).

The mechanical properties of the material are the Young's modulus $E = 1000 \text{ MPa}$, the Poisson's ratio $\nu = 0$, and the fracture toughness $g_c = 1 \text{ MPa}\cdot\text{s}$.

We impose zero displacements on the external boundary of Ω . Also we set $d = 1$ on prescribed (initial) fracture and $d = 0$ on the external boundary of Ω . A monotonically increasing pressure is applied on the upper and lower faces of fracture with the magnitude $p = 1 \text{ MPa}$. Figure 8 depicts the geometry and boundary conditions.

Bourdin *et al.* [33] proposed a formula to compute the fracture aperture as:

$$w = \mathbf{u} \cdot \mathbf{n}_\Gamma \simeq \int_s \mathbf{u} \cdot \nabla d \, dx.$$

Then, the fracture volume is calculated by integrating the fracture aperture along the fracture's path:

$$V_f = \int_\Gamma w \, ds \simeq \int_\Omega \mathbf{u} \cdot \nabla d \, d\Omega.$$

Figure 9 shows the aperture profile for different h and ℓ . The dash line in black represents the Sneddon's analytical solution [57]. Also, the crack volume computed by Sneddon's analytical solution and our numerical tests are summarized in Table 3.

Table 3: Crack volumes for different ℓ for numerical tests and analytical solution ($h = 4\text{mm}$).

ℓ (mm)	1.4×10^2	1.2×10^2	1.0×10^2
Numerical fracture volume (mm^2)	2.89×10^2	2.75×10^2	2.60×10^2
Analytical fracture volume (mm^2)	2.51×10^2		

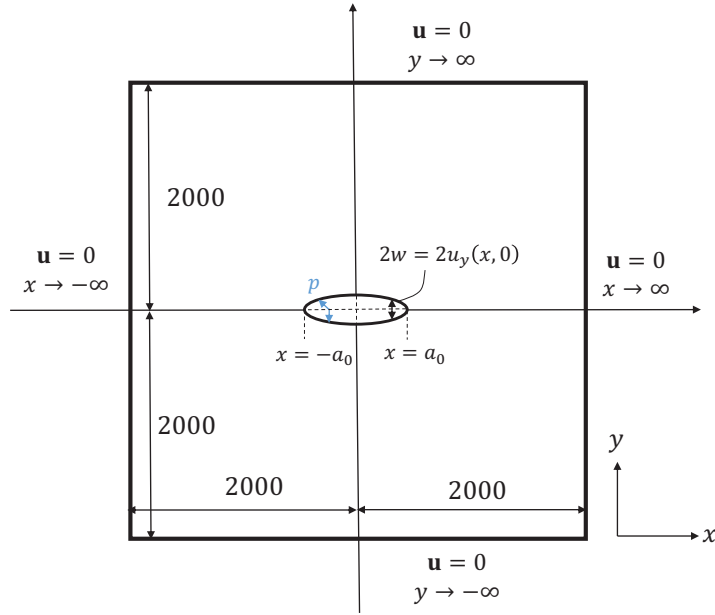


Figure 8: Computation of the crack opening displacement. Schematic view of the deformed line crack in a two dimensional domain.

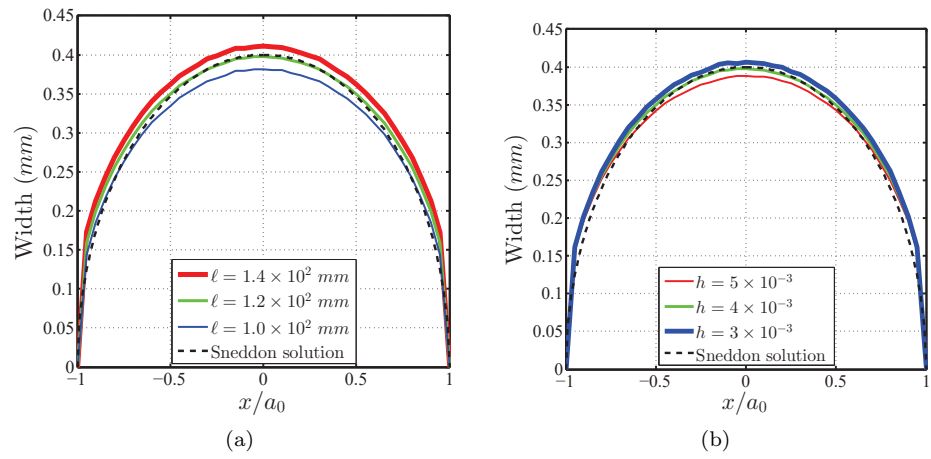


Figure 9: Computation of the crack opening displacement. We output the results for (9a) various ℓ with $h = 4$ mm and (9b) various h with $\ell = 1.2 \times 10^2$ mm, and compare them with Sneddon's analytical solution [57].

4.4. Increasing pressure leading to joining fractures

This example motivated by Wheeler *et al.* [58] demonstrates one major capability of the phase field approach that there is no need to track any complicated fracture geometry for joining fractures.

Consider a computational domain of $\Omega = (0, 4.0) \times (0, 4.0)$ (unit: m by m) containing two pre-existing line fractures with a length of $2a_0 = 0.4$ m, more precisely, $\mathcal{C}_h = [1.8, 2.2] \times \{0\}$ and $\mathcal{C}_v = \{2.6\} \times [1.8, 2.2]$. To minimize the effect of the boundary conditions on the results, the domain size is much bigger than the fracture length ($L \gg 2a_0$). A discretization with 19,368 standard P_1 elements is applied such that an effective element size of $h \approx 20$ mm is obtained in the critical zone. Also, let $\ell = 2h$. Figure 10 depicts the geometric setup. A zero displacement is imposed on the boundary. Also, we set $d = 1$ for the prescribed (initial) fractures, and $d = 0$ on the boundary. A monotonically increasing pressure is applied on the upper and lower faces of the fracture with the magnitude $p = m\bar{p}$ where $\bar{p} = 0.01$ MPa and $m = 1, 2, \dots, 115$.

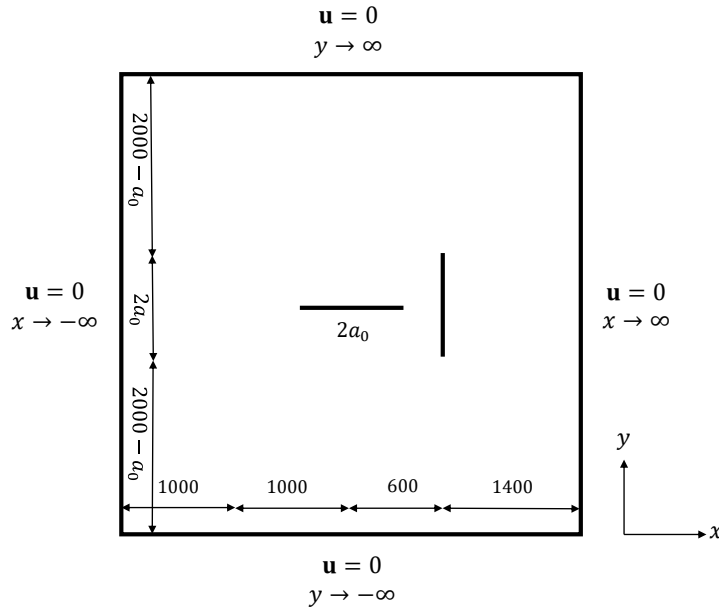


Figure 10: Schematic of a square plate (unit: mm) with two pre-existing fractures. A monotonically increasing pressure with constant increments $p = m\bar{p}$ is applied on the fracture faces.

Following [58], we adopt the values of the material parameters given in Table 4.

Figure 11 shows the phase field evolution at different load steps: (11a) $m = 1$, (11b) $m = 113$, (11c) $m = 114$, and (11d) $m = 115$. The results show that the horizontal fracture starts to propagate at $m = 113$, and at $m = 114$ it intersects the vertical fracture. Overall speaking the fracture paths agree with those in [58]. Note the fracture propagation is unstable in this example.

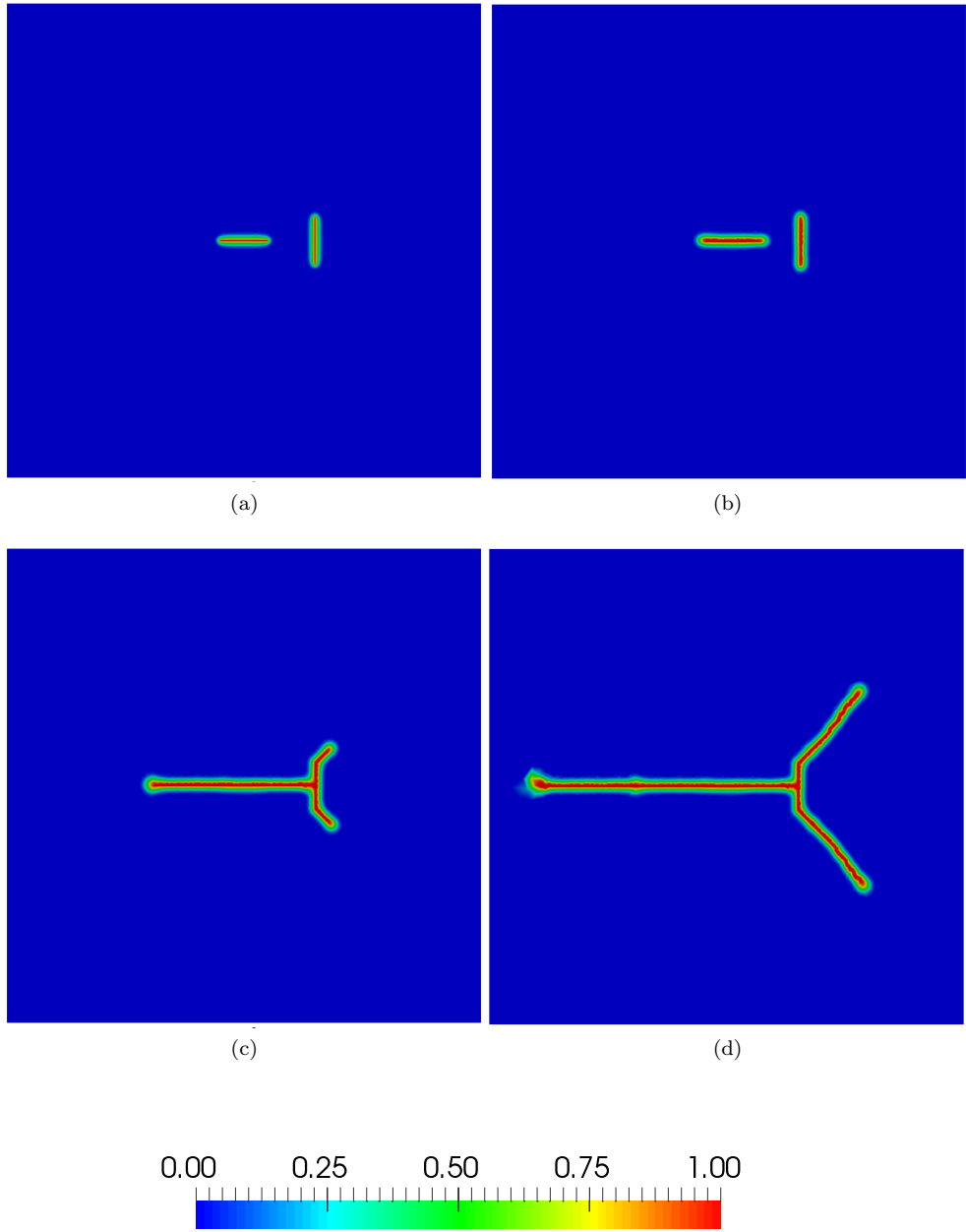


Figure 11: Increasing pressure leading to joining fractures ($p = m\bar{p}$). Phase field contours at different load steps (11a) $m = 1$, (11b) $m = 113$, (11c) $m = 114$, and (11d) $m = 115$. The results show that the horizontal fracture starts to propagate at $m = 113$, and at $m = 114$ it intersects the vertical fracture.

Table 4: Increasing pressure leading to joining fractures: Material parameters [58]

Parameters	symbol	unit	value
Young's modulus	E	MPa	1.0
Poisson's ratio	ν	—	0.2
Critical energy release rate	g_c	MPa·mm	1.0

4.5. CO_2 -driven fracture

In this example, we investigate the fracture propagation in a square plate with a pressurized CO_2 flow, with [10, 11] as the benchmarks. The specimen has edge lengths of $L = 170$ mm. The geometric setup and boundary conditions are depicted in Figure 12. The sample is discretized into 4,832 three-noded triangular elements so that the mesh size $h \approx 5.68$ mm is obtained. Also, we set $\ell = 1.6$ mm. Table 5 shows the remaining parameters to be input.

$$\mathbf{u} = \mathbf{u}_D, p = p_D$$

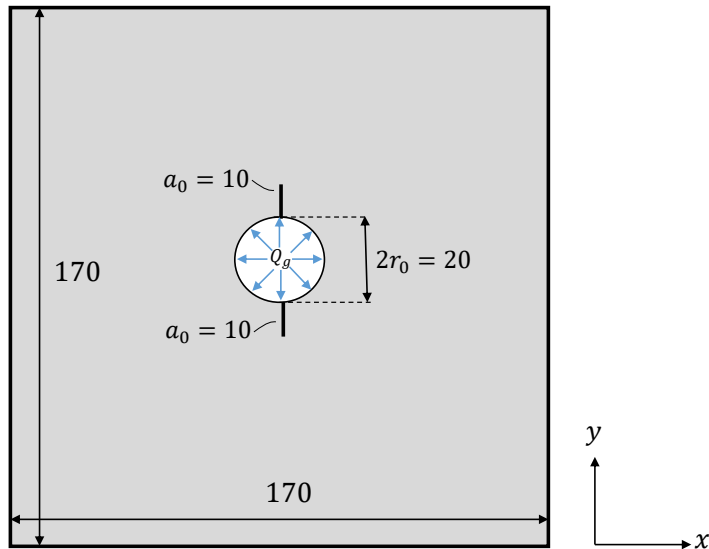


Figure 12: Schematic of a fractured square plate (unit: mm) with pressurized CO_2 flow.

As in Figure 12, there exist two preexisting fractures representing the perforations. We set $d = 1$ for both fractures and set the Dirichlet boundary condition $d = 0$ on the external boundary. The fluid is continuously injected into the central borehole with diameter $2r_0 = 20$ mm, until after the fractures propagate. Note that in this problem, the isothermal condition is adopted so that CO_2 is in the supercritical phase ($T = 45^\circ C$).

For the sake of simplicity, the *in situ* stress $\sigma_1 = \sigma_3 = 1$ MPa is imposed on the boundary by means of its “equivalent” prescribed displacement. More precisely, the displacement of the same specimen with no fracture under the

same *in situ* stress is first computed, then used as the Dirichlet boundary condition for the problem at hand. On the external boundary, we set $p = p_D$ where $p_D = 0$. Moreover, $\Gamma_P = \Gamma_D$ in this example.

Table 5: Default parameter values for the example. These values are taken from [11] except g_c , which is from (6).

Parameters	symbol	unit	value
Young's modulus	E	MPa	6×10^3
Poisson's ratio	ν	—	0.34
Critical energy release rate	g_c	MPa·mm	0.306
Biot coefficient	α	—	0.85
Porosity	ϕ	—	0.01
Initial permeability	k_0	mm ²	1×10^{-12}
Dynamic viscosity of CO ₂	μ	MPa·s	4.04×10^{-11}
Initial pressure	p_0	MPa	0.1
Rock's tensile strength	σ_T	MPa	11

Figure 13 shows the evolution of phase field diagram (left) and pressure profile (right) at different time steps. As seen, the fractures propagate along a straight line, and the pressure profile is accordingly distributed with the highest gradient around the borehole.

Next, we aim to calculate the breakdown pressure p_b , the pressure value when the fractures start to propagate. Figure 14 illustrates the pressure evolution at the top of the borehole and the fracture length function. To estimate the breakdown pressure, first we output the fracture length with regard to (2). Then, we obtain the time when the slope suddenly changes in the fracture length function (C_ℓ), which is the time corresponding to the breakdown pressure (here $t \approx 0.72t_f$). Hence the breakdown pressure reads $p_b = 10.9$ MPa. This value for p_b is in agreement with H-F and H-W analytical solutions. Also, our results agree with experiments results of Ishida *et al.* [9] within 30%, see Table 6 and the next paragraph for more elaborations.

Table 6: Breakdown pressure of numerical test and analytical solutions for $\sigma_1 = \sigma_3 = 1$ MPa.

	Numerical	H-F solution	H-W solution	Experimental [9]
p_b (MPa)	10.9	11	9.1	8.44

360

Classical solutions of breakdown pressure. There exist two classical expressions to calculate the breakdown pressure. In the case without poroelastic effect the rock deformation does not penetrate into the pressurized fracture, the Hubbert-Willis (H-W) solution applies [59]:

$$p_b = 3\sigma_3 - \sigma_1 + \sigma_T,$$

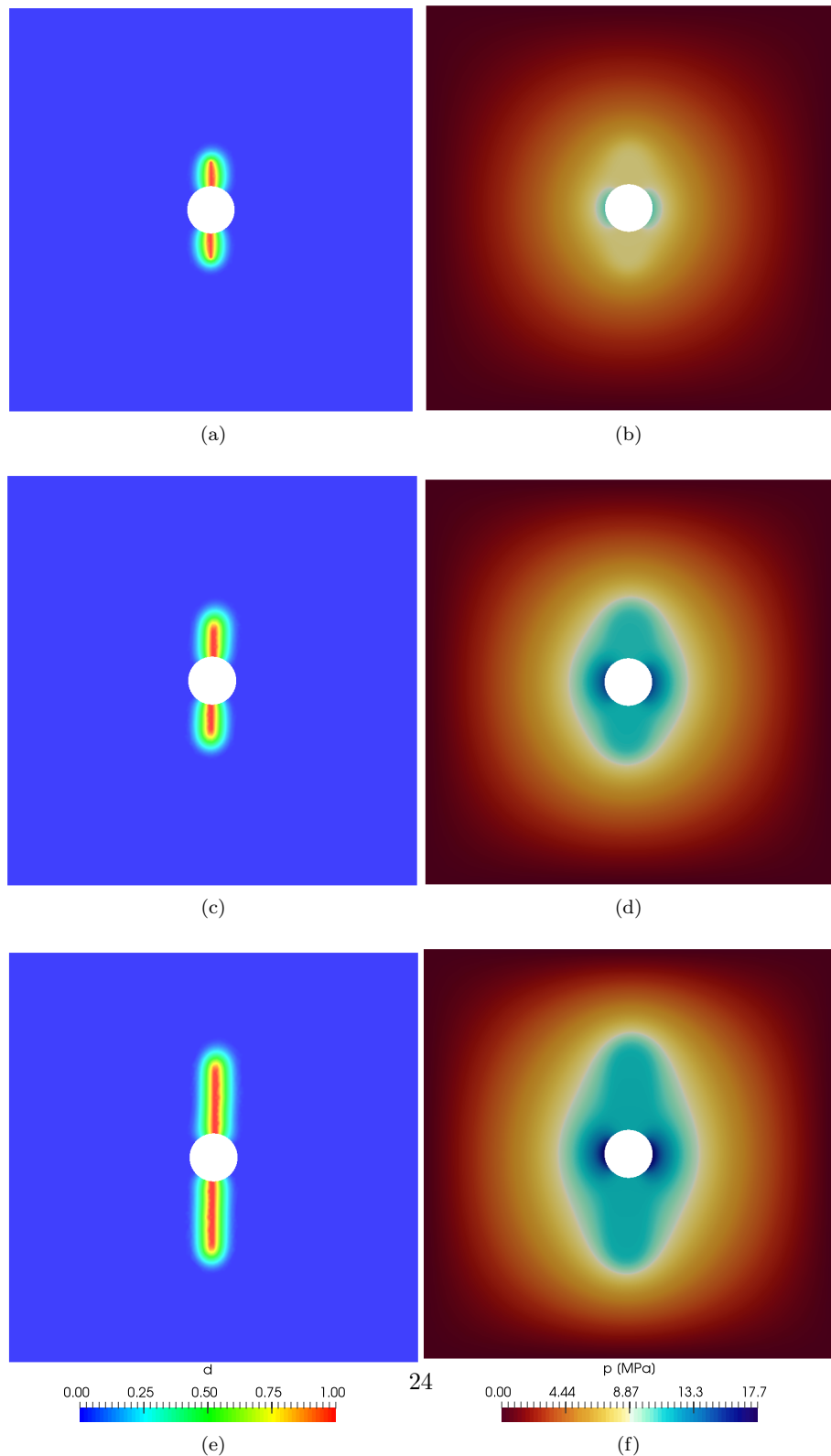


Figure 13: Left: Phase field diagram at different stages (13a) $t = 0.5t_f$, (13c) $t = 0.74t_f$, and (13e) $t = t_f$. Right: Pressure profile at (13b) $t = 0.5t_f$, (13d) $t = 0.74t_f$, and (13f) $t = t_f$.

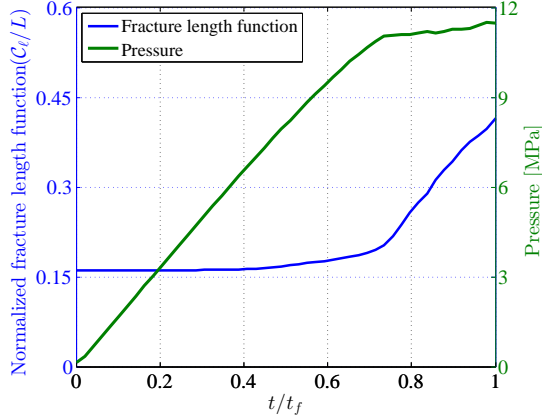


Figure 14: The pressure at the top of the borehole (green line), and the fracture length function (blue line) as functions of time. The time when there is a sudden change of slope in C_ℓ assumes the time corresponding to the breakdown pressure ($t = 0.72t_f$) and the corresponding breakdown pressure is $p_b = 10.9$ MPa. This is in agreement with H-F and H-W analytical solutions.

in which the rock is assumed to be an elastic medium. When the porous medium is set, the Haimson-Fairhurst (H-F) solution is preferred [60]:

$$p_b = \frac{3\sigma_3 - \sigma_1 + \sigma_T + p_0}{1 + \frac{\nu}{1-\nu}\alpha},$$

where we denote by p_b the breakdown fluid pressure, σ_3 , and σ_1 are the minimum and maximum principal stresses, respectively, and σ_T is the rock's tensile strength.

Effect of N , h , and ℓ on the breakdown pressure. Here we aim to study how the number of time steps N , the mesh size h , and the regularization length scale ℓ affect the value of breakdown pressure. As seen in Figure 15, the plots show similar numerical results for the pressure evolution.

Breakdown pressure result of an anisotropic in situ stress. In this example we set the maximum ($\sigma_1 = 3$ MPa) and minimum ($\sigma_3 = 2$ MPa) *in situ* stress. The other input data and boundary conditions are the same as aforementioned.

The pressure at the top of the borehole and the fracture length function, (2), at different stages are illustrated in Figure 16. The breakdown time ($t \approx 0.77t_f$) and the corresponding breakdown pressure is $p_b = 11.9$ MPa, see Table 7.

Table 7: Breakdown pressure of numerical test and analytical solutions for $\sigma_1 = 3$ MPa and $\sigma_3 = 2$ MPa.

	Numerical	H-F solution	H-W solution
p_b (MPa)	11.9	14	9.8

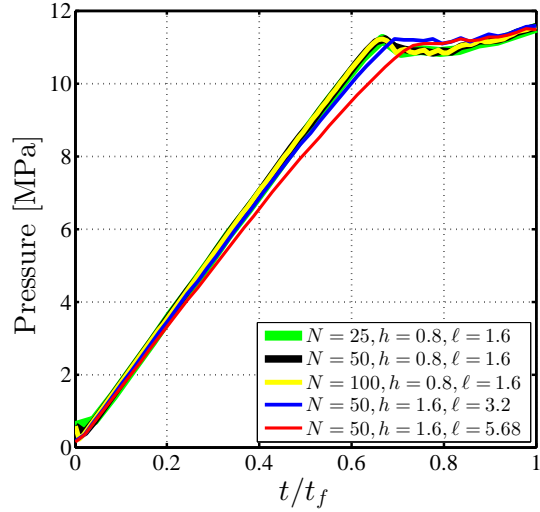


Figure 15: Evolution of the pressure at the top of the borehole for different numbers of time steps N , mesh size h , and ℓ .

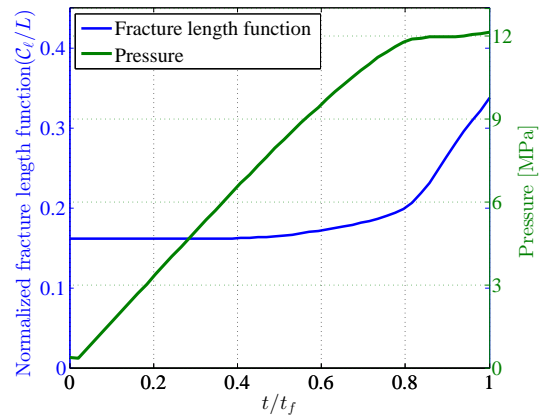


Figure 16: The pressure at the top of the borehole (green line) and the fracture length function (blue line) versus time for deviatoric *in situ* stress are shown. The time ($t \approx 0.8t_f$) when there is a change of slope in the fracture length function (C_ℓ) should correspond to the breakdown pressure ($p_b = 11.9$ MPa).

Effect of dynamic viscosity on breakdown pressure. We conduct several numerical examples to investigate the effect of dynamic viscosity μ on the breakdown pressure p_b . In this set of examples an effective mesh size, the mesh size near the borehole or the fractures, $h \approx 1.6$ mm is adopted. Also, we set $\ell = 2h$. In Figure 17 we plot the pressure evolution up to the time when $C_\ell(t)$ changes slope, so that the end points correspond to the breakdown pressures. The results indicate that p_b is approximately the same for different fluid viscosities, but the time when breakdown pressure reaches is different. Figure 17 demonstrates that the rock will break earlier for the fluid with bigger dynamic viscosity. Also it shows that regardless of the fracturing fluid, the breakdown pressure is slightly the same for all cases. This is in accordance with the physics that the breakdown pressure normally reflects the strength of the solid. However, Wang *et al.* [11] reported different breakdown pressures for different fluids which also agrees with some experiments [9, 10]. We believe this discrepancy demands further research.

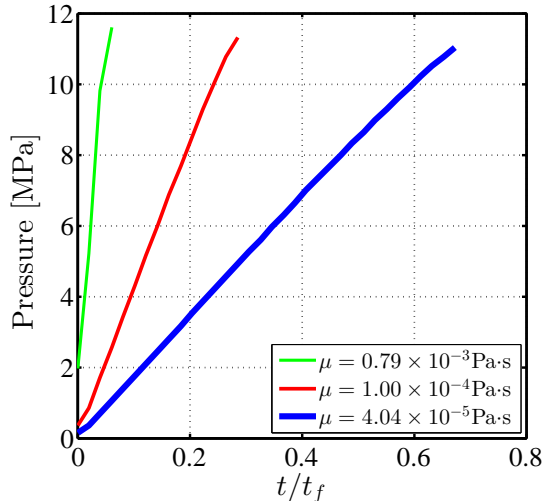


Figure 17: Evolution of the pressure at the top of the borehole for different μ 's. As seen, even though p_b is the same for different fracturing fluids, by increasing μ , the breakdown pressure is reached earlier.

4.6. Interaction between CO₂-driven fractures and natural fractures

In this example, we investigate the interaction between two CO₂-driven fractures and two inclined natural fractures. The specimen has edge lengths of $L = 170$ mm. The geometric setup and boundary conditions are depicted in Figure 18. The sample is discretized into 32,736 three-noded triangular elements so that the mesh size $h \approx 6.25 \times 10^{-1}$ mm is obtained. Also, we set $\ell = 4h$. The remaining input data can be found in Table 5.

As in Figure 18, there exist two pre-existing vertical fractures representing the perforations and two inclined natural fractures. We set $d = 1$ for both initial and inclined natural fractures, and the Dirichlet boundary condition $d = 0$ is

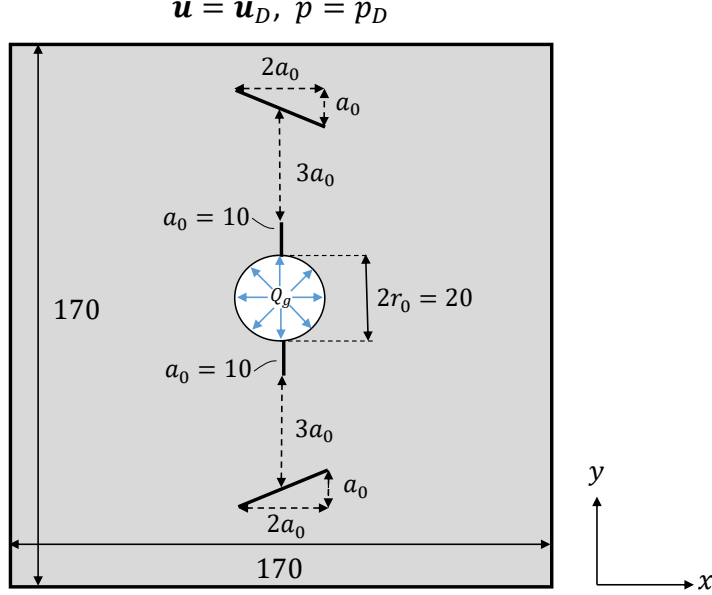


Figure 18: Interaction between CO₂-driven fracture and inclined natural fractures. The geometric setup and boundary conditions are shown (unit: mm). There exist two CO₂-driven fractures and two inclined natural ones.

imposed on the external boundaries. The fluid is continuously injected into the central borehole with diameter $2r_0 = 20$ mm. The *in situ* stress with the value of $\sigma_1 = \sigma_3 = 1$ MPa is also imposed on the boundary by means of its ‘equivalent’ prescribed displacement. See Section 4.5 for more descriptions.

Figure 19 shows the evolution of the phase field profile (left) and the pressure profile (right) at different time steps. As seen, the vertical fractures propagate along a straight line until $t = 0.4t_f$. Then, near the inclined natural fractures, the CO₂-driven fractures turns to join them with an angle of approximately 90° at $t = 0.8t_f$. In the last frame 19g, the vertical fractures deviate into the inclined natural fractures and propagate from left tips. This fracture evolving pattern is called ‘crossing with an offset’ which is one possible interaction process of hydraulic fracture and natural fracture [61].

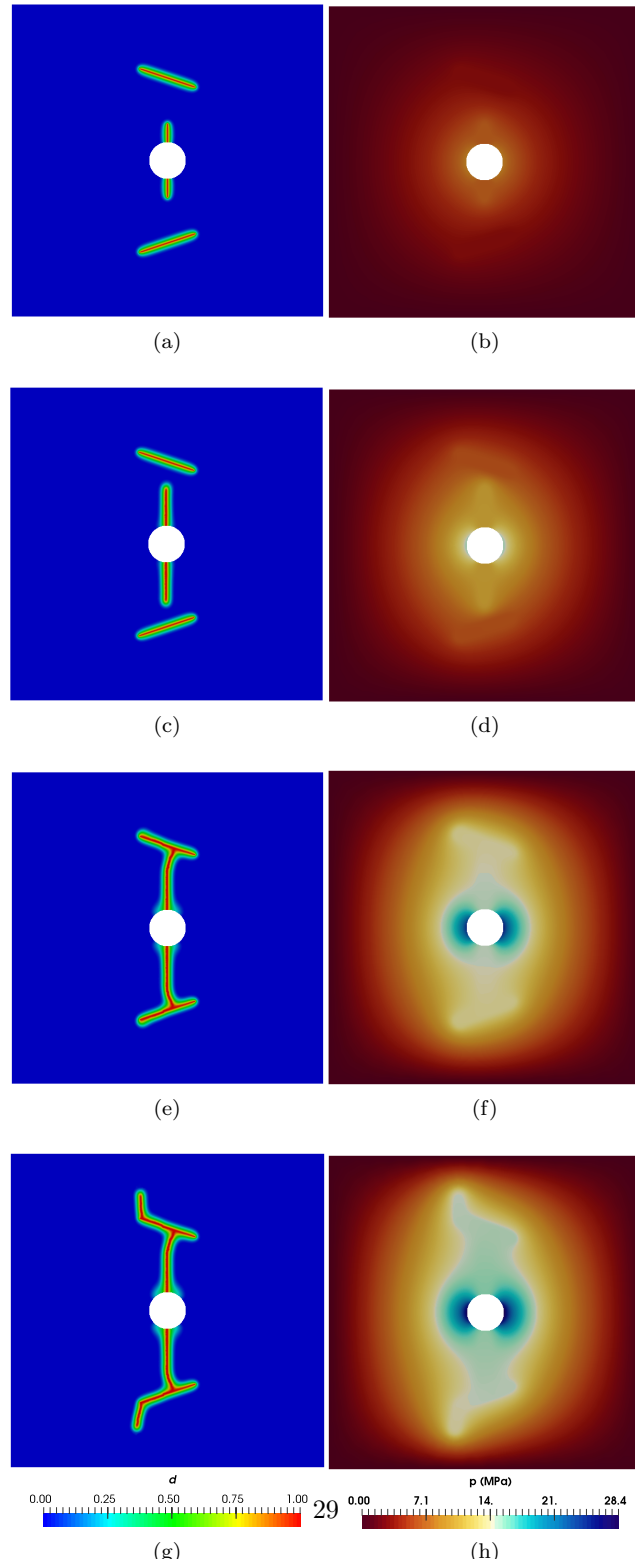


Figure 19: Left: Phase field diagram at different stages (19a) $t = 0.$, (19c) $t = 0.4t_f$, (19e) $t = 0.8t_f$, and (19g) $t = t_f$. Right: Pressure profile at (19b) $t = 0.$, (19d) $t = 0.4t_f$, (19f) $t = 0.8t_f$, and (19h) $t = t_f$. As seen, the vertical fractures propagate along a straight line until they reached the natural fractures. Then, they deviate into the inclined natural fractures, and continue evolving from left tips. ‘Crossing with an offset’ is one possible interaction process of hydraulic fracture and natural fracture [61].

⁴¹⁰ **5. Conclusions**

We have proposed [and verified](#) a phase field approach to simulate CO₂ fracturing, with CO₂ treated as a compressible fluid. [In one of the numerical examples, the](#)[The](#) breakdown pressure agrees well with widely used analytical solutions. Also, the results agree with experimental results within 30%. While
⁴¹⁵ this work represents the first of its kind, potentially the phase field approach allows complicated modeling of fracture initiation and branching.

AppendixA. Weak forms and discretized formulations

Here we provide weak forms useful for FEniCS implementation.

AppendixA.1. Porous medium

To proceed, let the test function spaces be

$$\begin{aligned}\mathcal{V}_u &:= \{\bar{\mathbf{u}} \in H^1(\Omega; \mathbb{R}^2) \mid \bar{\mathbf{u}} = \mathbf{0} \text{ on } \Gamma_D\}, \\ \mathcal{V}_d &:= H^1(\Omega).\end{aligned}$$

Then we derive the first variations of the energy functional (3), which will be needed for stating the weak form:

$$\begin{aligned}\delta\Pi_\ell [(\mathbf{u}, d); \bar{\mathbf{u}}] &:= \int_{\Omega} \boldsymbol{\sigma}[\boldsymbol{\varepsilon}(\mathbf{u}), d] : \boldsymbol{\varepsilon}(\bar{\mathbf{u}}) d\Omega - \int_{\Gamma_N} \mathbf{t}_N \cdot \bar{\mathbf{u}} d\Gamma - \int_{\Omega} \mathbf{b} \cdot \bar{\mathbf{u}} d\Omega \\ &\quad + \int_{\Omega} (\alpha - 1) \nabla ((1 - d)^2 p) \cdot \bar{\mathbf{u}} d\Omega + \int_{\Omega} (1 - d)^2 \nabla p \cdot \bar{\mathbf{u}} d\Omega\end{aligned}\tag{A.1a}$$

$$\begin{aligned}\delta\Pi_\ell [(\mathbf{u}, d); \bar{d}] &:= \int_{\Omega} (\alpha - 1) g'(d) \bar{d} p \operatorname{div} \mathbf{u} d\Omega + \int_{\Omega} g'(d) \bar{d} \nabla p \cdot \mathbf{u} d\Omega \\ &\quad + \int_{\Omega} g'(d) \psi_+(\boldsymbol{\varepsilon}) \bar{d} d\Omega + \frac{g_c}{4c_w} \int_{\Omega} \left(\frac{\omega'(d) \bar{d}}{\ell} + 2\ell \nabla d \cdot \nabla \bar{d} \right) d\Omega.\end{aligned}\tag{A.1b}$$

⁴²⁰ The weak form can thus be stated as: Find $(\mathbf{u} \times d) \in \mathcal{S}_{\mathbf{u}} \times \mathcal{S}_d$, such that for all admissible functions $(\bar{\mathbf{u}} \times \bar{d}) \in \mathcal{V}_{\mathbf{u}} \times \mathcal{V}_d$, $\delta\Pi_\ell [(\mathbf{u}, d); \bar{\mathbf{u}}] = 0$ and $\delta\Pi_\ell [(\mathbf{u}, d); \bar{d}] = 0$.

Also we take another variation from (3) which will be needed for the discretized formulation:

$$\delta^2\Pi_\ell [(\mathbf{u}, d); \bar{\mathbf{u}}, \delta\mathbf{u}] = \int_{\Omega} \boldsymbol{\varepsilon}(\delta\mathbf{u}) : \mathbb{C}[\boldsymbol{\varepsilon}(\mathbf{u}), d] : \boldsymbol{\varepsilon}(\bar{\mathbf{u}}) d\Omega,\tag{A.2a}$$

$$\begin{aligned}\delta^2\Pi_\ell [(\mathbf{u}, d); \bar{d}, \delta d] &= \int_{\Omega} \delta d g''(d) \psi_+(\boldsymbol{\varepsilon}) \bar{d} d\Omega \\ &\quad + \int_{\Omega} (\alpha - 1) g''(d) \bar{d} \delta d p \operatorname{div} \mathbf{u} d\Omega + \int_{\Omega} g''(d) \bar{d} \delta d \nabla p \cdot \mathbf{u} d\Omega \\ &\quad + \frac{g_c}{4c_w} \int_{\Omega} \left[\frac{\delta d w''(d) \bar{d}}{\ell} + 2\ell \nabla(\delta d) \cdot \nabla \bar{d} \right] d\Omega,\end{aligned}\tag{A.2b}$$

where the fourth-order tensor $\mathbb{C}[\boldsymbol{\varepsilon}(\mathbf{u}), d] = \frac{\partial \boldsymbol{\sigma}(\boldsymbol{\varepsilon}, d)}{\partial \boldsymbol{\varepsilon}} \Big|_{\boldsymbol{\varepsilon}=\boldsymbol{\varepsilon}(\mathbf{u})}$ is the tangent elasticity tensor.

To discretize the problem, we divide Ω with a conforming mesh \mathcal{T}_h of triangular elements. Let η be the set of nodes of \mathcal{T}_h . We approximate (\mathbf{u}, d) with the standard P_1 finite element basis functions associated with all nodes $i \in \eta$:

$$\mathbf{u}(\mathbf{x}) = \sum_{i \in \eta} \mathbf{N}_i^{\mathbf{u}}(\mathbf{x}) \mathbf{u}_i, \quad d(\mathbf{x}) = \sum_{i \in \eta} N_i(\mathbf{x}) d_i,\tag{A.3}$$

where \mathbf{u}_i , and d_i are the displacement and phase field values at node i , respectively; and \mathbf{N}_i^u is given by:

$$\mathbf{N}_i^u = \begin{bmatrix} N_i & 0 \\ 0 & N_i \end{bmatrix},$$

425 where N_i is the standard finite element shape function associated with $i \in \eta$, satisfying $N_j(\mathbf{x}_i) = \delta_{ji}$, for all $i, j \in \eta$, and $\mathbf{x}_i, \mathbf{u}_i \in \mathbb{R}^2$ are the position vector and nodal displacement vector of node i , respectively. Note that we also apply the same discretization to the test functions.

Discretized weak form. Let n_{nodes} denote the number of nodes in η . Let $\mathbf{u} \in \mathbb{R}^{2n_{\text{nodes}}}$, $\mathbf{d} \in \mathbb{R}^{n_{\text{nodes}}}$ contain all entries of \mathbf{u}_i , d_i , respectively, for all $i \in \eta$. The discretized residuals can be written as $\mathbb{U}_i(\mathbf{u}) := \delta\Pi(\mathbf{u}; \mathbf{N}_i^u) \in \mathbb{R}^2$ and $\mathbb{D}_i(d) := \delta\Pi(d; N_i) \in \mathbb{R}$ for all $i \in \eta$. With (A.1), these residual vectors are expressed as follows:

$$\begin{aligned} \mathbb{U}_i &= \int_{\Omega} (\mathbf{B}_i)^T \boldsymbol{\sigma}[\boldsymbol{\varepsilon}(\mathbf{u}), d] d\Omega - \int_{\Gamma_N} (\mathbf{N}_i^u)^T \mathbf{t}_N d\Gamma - \int_{\Omega} (\mathbf{N}_i^u)^T \mathbf{b} d\Omega \\ &\quad + \int_{\Omega} (\alpha - 1)(\mathbf{N}_i^u)^T \nabla((1-d)^2 p) d\Omega + \int_{\Omega} (\mathbf{N}_i^u)^T (1-d)^2 \nabla p d\Omega \\ \mathbb{D}_i &= \int_{\Omega} (\alpha - 1) g'(d) N_i p \operatorname{div} \mathbf{u} d\Omega + \int_{\Omega} g'(d) N_i (\nabla p)^T \mathbf{u} d\Omega \\ &\quad + \int_{\Omega} g'(d) \psi_+(\boldsymbol{\varepsilon}) N_i d\Omega + \frac{g_c}{4c_w} \int_{\Omega} \left(\frac{w'(d) N_i}{\ell} + 2\ell \nabla d \cdot \nabla N_i \right) d\Omega, \end{aligned} \quad (\text{A.4})$$

where \mathbb{U}_i is also called the nodal force at i . Also note that in (A.4), $\boldsymbol{\sigma}$ is understood as a 3-vector, and the strain-displacement matrix for node i are given by:

$$\mathbf{B}_i = \begin{bmatrix} N_{i,x} & 0 \\ 0 & N_{i,y} \\ N_{i,y} & N_{i,x} \end{bmatrix}.$$

The discretized weak form is $\mathbb{U}_i = \mathbf{0}$ for all nodes i at which \mathbf{u} is not prescribed, and $\mathbb{D}_i = 0$ for all nodes i at which d is not prescribed.

Tangent stiffness matrices. The tangent stiffness matrices are needed for Newton-Raphson algorithms. The tangent stiffness matrix components of (A.2) are $\mathbf{K}_{ij}^u := \partial \mathbb{U}_i / \partial \mathbf{u}_j = \delta^2 \Pi[\mathbf{u}; \mathbf{N}_i^u, \mathbf{N}_j^u] \in \mathbb{R}^{2 \times 2}$ for all $i, j \in \eta$ and $K_{ij}^d := \partial \mathbb{D}_i / \partial d_j = \delta^2 \Pi[d; N_i, N_j] \in \mathbb{R}$ for all $i, j \in \eta$, which can be expressed as follows:

$$\mathbf{K}_{ij}^u = \int_{\Omega} (\mathbf{B}_i)^T \mathbf{D} \mathbf{B}_j d\Omega, \quad (\text{A.5a})$$

$$\begin{aligned} K_{ij}^d &= \int_{\Omega} (\alpha - 1) g''(d) N_i N_j p \operatorname{div} \mathbf{u} d\Omega + \int_{\Omega} g''(d) N_i N_j (\nabla p)^T \mathbf{u} d\Omega \\ &\quad + \int_{\Omega} g''(d) \psi_+(\boldsymbol{\varepsilon}) N_i N_j d\Omega + \frac{g_c}{4c_w} \int_{\Omega} \left[\frac{w''(d) N_i N_j}{\ell} + 2\ell (\nabla N_i)^T \nabla N_j \right] d\Omega, \end{aligned} \quad (\text{A.5b})$$

where we denote by \mathbf{D} the matrix form of the tangent elastic modulus tensor \mathbb{C} . Below we give its expression $\mathbf{D} = g(d)\mathbf{D}_+ + \mathbf{D}_-$ for our adopted tension-compression decomposition [34]:

$$\begin{aligned}\mathbf{D}_+ &= BH(\text{tr } \boldsymbol{\varepsilon}) \begin{bmatrix} 1 & 1 & 0 \\ 1 & 1 & 0 \\ 0 & 0 & 0 \end{bmatrix} + \frac{G}{3} \begin{bmatrix} 4 & -2 & 0 \\ -2 & 4 & 0 \\ 0 & 0 & 3 \end{bmatrix}, \\ \mathbf{D}_- &= BH(-\text{tr } \boldsymbol{\varepsilon}) \begin{bmatrix} 1 & 1 & 0 \\ 1 & 1 & 0 \\ 0 & 0 & 0 \end{bmatrix},\end{aligned}$$

where $B = E/[3(1-2\nu)]$ is the bulk modulus. Here, H is the Heaviside function such that $H(a) = 1$ if $a > 0$, $H(a) = 0$ if $a < 0$, and $H(a) = \frac{1}{2}$ if $a = 0$.

Appendix A.2. Compressible (CO_2) fluid flow discretization

The compressible fluid flow discretization is also done via the finite element method. We first discretize in time and then in space. We will adopt the backward Euler method for time discretization.

To proceed, let the admissible set of pressure be:

$$\mathcal{S}_p := \{p \in H^1(\Omega) | p = p_D \text{ on } \Gamma_P\}.$$

The test function space can be defined as:

$$\mathcal{V}_p := \{\bar{p} \in H^1(\Omega) | \bar{p} = 0 \text{ on } \Gamma_P\}.$$

The weak form can be stated as: find $p \in \mathcal{S}_p$ such that for all admissible functions $\bar{p} \in \mathcal{V}_p$,

$$\begin{aligned}&\frac{1}{\Delta t} \int_{\Omega} \phi(\rho - \rho^{n-1}) \bar{p} \, d\Omega + \frac{1}{\Delta t} \int_{\Omega} \rho(\varepsilon_v - \varepsilon_v^{n-1}) \bar{p} \, d\Omega \\ &+ \int_{\Omega} \rho \frac{k(d)}{\mu} \nabla p \cdot \nabla \bar{p} \, d\Omega - \int_{\Gamma_B} Q_g \bar{p} \, d\Gamma = 0,\end{aligned}\tag{A.6}$$

where ρ^{n-1} and ε_v^{n-1} denote solutions at the previous time step.

Also, we use the conventional finite element shape functions $\{N_i\}$ for p :

$$p(\mathbf{x}) = \sum_{i \in \eta} p_i N_i(\mathbf{x}).\tag{A.7}$$

Thus, the residual vector form of A.6 is expressed as follows:

$$\begin{aligned}\mathbb{P}_i &:= \frac{1}{\Delta t} \int_{\Omega} \phi(\rho - \rho^{n-1}) N_i \, d\Omega + \frac{1}{\Delta t} \int_{\Omega} \rho(\varepsilon_v - \varepsilon_v^{n-1}) N_i \, d\Omega \\ &+ \int_{\Omega} \rho \frac{k(d)}{\mu} (\nabla p)^T \nabla N_i \, d\Omega - \int_{\Gamma_B} Q_g N_i \, d\Gamma.\end{aligned}\tag{A.8}$$

The discretized weak form is $\mathbb{P}_i = 0$ for all nodes i at which p is not prescribed.

The tangent stiffness matrix form of the fluid flow $K_{ij}^p := \partial \mathbb{P}_i / \partial p_j$ for all $i, j \in \eta$, which can be expressed as follows:

$$K_{ij}^p := \int_{\Omega} \rho \frac{k(d)}{\mu} (\nabla N_i)^T \nabla N_j \, d\Omega.\tag{A.9}$$

Acknowledgments

440 This work is supported by the National Natural Science Foundation of China with grant #11402146. YS also acknowledges the financial support by the Young 1000 Talent Program of China.

- 445 [1] G. Hattori, J. Trevelyan, C. E. Augarde, W. M. Coombs, A. C. Aplin, Numerical simulation of fracking in shale rocks: Current state and future approaches, *Archives of Computational Methods in Engineering* 24 (2) (2017) 281–317.
- 450 [2] R. Middleton, H. Viswanathan, R. Currier, R. Gupta, CO₂ as a fracturing fluid: Potential for commercial-scale shale gas production and CO₂ sequestration, *Energy Procedia* 63 (2014) 7780–7784.
- 455 [3] L. Wang, B. Yao, M. Cha, N. B. Alqahtani, T. W. Patterson, T. J. Kneafsey, J. L. Miskimins, X. Yin, Y.-S. Wu, Waterless fracturing technologies for unconventional reservoirs—opportunities for liquid nitrogen, *Journal of Natural Gas Science and Engineering* 35 (2016) 160–174.
- 460 [4] J. Miller, R. T. Johansen, Fracturing oil shale with explosives for in situ recovery, *Shale Oil, Tar Sands, and Related Fuel Sources* (1976) 98–111.
- 465 [5] A. T. Lillies, S. R. King, Sand fracturing with liquid carbon dioxide, in: SPE Production Technology Symposium, Society of Petroleum Engineers, 1982, pp. SPE-11341-MS.
- [6] Y. Suehiro, M. Nakajima, K. Yamada, M. Uematsu, Critical parameters of $\{x\text{CO}_2 + (1-x)\text{CHF}_3\}$ for $x=(1.0000, 0.7496, 0.5013, \text{ and } 0.2522)$, *The Journal of Chemical Thermodynamics* 28 (10) (1996) 1153–1164.
- 470 [7] D. W. Brown, A hot dry rock geothermal energy concept utilizing supercritical CO₂ instead of water, in: Proceedings of the twenty-fifth workshop on geothermal reservoir engineering, Stanford University, 2000, pp. 233–238.
- [8] R. S. Middleton, J. W. Carey, R. P. Currier, J. D. Hyman, Q. Kang, S. Karra, J. Jiménez-Martínez, M. L. Porter, H. S. Viswanathan, Shale gas and non-aqueous fracturing fluids: Opportunities and challenges for supercritical CO₂, *Applied Energy* 147 (2015) 500–509.
- 475 [9] T. Ishida, K. Aoyagi, T. Niwa, Y. Chen, S. Murata, Q. Chen, Y. Nakayama, Acoustic emission monitoring of hydraulic fracturing laboratory experiment with supercritical and liquid CO₂, *Geophysical Research Letters* 39 (16) (2012) L16309.
- [10] T. Ishida, Y. Chen, Z. Bennour, H. Yamashita, S. Inui, Y. Nagaya, M. Naoi, Q. Chen, Y. Nakayama, Y. Nagano, Features of CO₂ fracturing deduced from acoustic emission and microscopy in laboratory experiments, *Journal of Geophysical Research: Solid Earth* 121 (11) (2016) 8080–8098.

- [11] J. Wang, D. Elsworth, Y. Wu, J. Liu, W. Zhu, Y. Liu, The influence of fracturing fluids on fracturing processes: A comparison between water, oil and SC-CO₂, *Rock Mechanics and Rock Engineering* 51 (1) (2018) 299–313.
- 480 [12] X. Zhou, T. J. Burbey, Fluid effect on hydraulic fracture propagation behavior: A comparison between water and supercritical CO₂-like fluid, *Geofluids* 14 (2) (2014) 174–188.
- [13] D. Ngo, A. C. Scordelis, Finite element analysis of reinforced concrete beams, *International Concrete Abstracts Portal* 64 (3) (1967) 152–163.
- 485 [14] N. Moës, J. Dolbow, T. Belytschko, A finite element method for crack growth without remeshing, *International Journal for Numerical Methods in Engineering* 46 (1) (1999) 131–150.
- 490 [15] R. Rangarajan, M. M. Chiaramonte, M. J. Hunsweck, Y. Shen, A. J. Lew, Simulating curvilinear crack propagation in two dimensions with universal meshes, *International Journal for Numerical Methods in Engineering* 102 (3-4) (2015) 632–670.
- [16] C. V. Verhoosel, M. A. Scott, T. J. Hughes, R. De Borst, An isogeometric analysis approach to gradient damage models, *International Journal for Numerical Methods in Engineering* 86 (1) (2011) 115–134.
- 495 [17] B. Bourdin, G. A. Francfort, J.-J. Marigo, Numerical experiments in revisited brittle fracture, *Journal of the Mechanics and Physics of Solids* 48 (4) (2000) 797–826.
- 500 [18] R. H. J. Peerlings, R. de Borst, W. A. M. Brekelmans, J. H. P. de Vree, Gradient enhanced damage for quasi-brittle materials, *International Journal for Numerical Methods in Engineering* 39 (19) (1996) 3391–3403.
- [19] G. A. Francfort, J.-J. Marigo, Revisiting brittle fracture as an energy minimization problem, *Journal of the Mechanics and Physics of Solids* 46 (8) (1998) 1319–1342.
- 505 [20] B. Bourdin, C. P. Chukwudzie, K. Yoshioka, A variational approach to the numerical simulation of hydraulic fracturing, in: SPE Annual Technical Conference and Exhibition, Society of Petroleum Engineers, 2012, pp. SPE-159154-MS.
- [21] A. Mikelić, M. F. Wheeler, T. Wick, Phase-field modeling of pressurized fractures in a poroelastic medium, *ICES Report* (2014) 14–18.
- 510 [22] K. Yoshioka, B. Bourdin, A variational hydraulic fracturing model coupled to a reservoir simulator, *International Journal of Rock Mechanics and Mining Sciences* 88 (2016) 137–150.
- [23] T. Wick, G. Singh, M. F. Wheeler, Fluid-filled fracture propagation with a phase-field approach and coupling to a reservoir simulator, *SPE Journal* 21 (03) (2016) 981–999.

- [24] S. Mauthe, C. Miehe, Hydraulic fracture in poro-hydro-elastic media, *Mechanics Research Communications* 80 (2017) 69–83.
- [25] W. Ehlers, C. Luo, A phase-field approach embedded in the theory of porous media for the description of dynamic hydraulic fracturing, *Computer Methods in Applied Mechanics and Engineering* 315 (2017) 348–368.
- [26] D. Culp, M. R. Tupek, P. Newell, M. H. Hubler, Phase-field modeling of fracture in CO₂ sequestration, in: 51st US Rock Mechanics/Geomechanics Symposium, American Rock Mechanics Association, 2017, pp. ARMA-2017-0644.
- [27] Y. Heider, B. Markert, Modelling of hydraulic fracturing and fluid flow change in saturated porous domains, *Proc. Appl. Math. Mech.* 17 (1) (2017) 95–98.
- [28] R. Span, W. Wagner, A new equation of state for carbon dioxide covering the fluid region from the triple-point temperature to 1100 K at pressures up to 800 MPa, *Journal of Physical and Chemical Reference Data* 25 (6) (1996) 1509–1596.
- [29] L. Ambrosio, V. M. Tortorelli, *On the Approximation of Free Discontinuity Problems*, Scuola Normale Superiore, 1990.
- [30] L. Ambrosio, V. M. Tortorelli, On the approximation of functionals depending on jumps by quadratic, elliptic functionals, *Bollettino dell’Unione Matematica Italiana* 6 (1992) 105–123.
- [31] E. Tanné, T. Li, B. Bourdin, J.-J. Marigo, C. Maurini, Crack nucleation in variational phase-field models of brittle fracture, *Journal of the Mechanics and Physics of Solids* 110 (2018) 80–99.
- [32] B. Bourdin, J.-J. Marigo, C. Maurini, P. Sicsic, Morphogenesis and propagation of complex cracks induced by thermal shocks, *Physical Review Letters* 112 (2014) 014301.
- [33] B. Bourdin, C. Chukwudzie, K. Yoshioka, A variational approach to the numerical simulation of hydraulic fracturing, in: M. Jirásek, O. Allix, N. Moës, J. Oliver (Eds.), *Computational Modeling of Fracture and Failure of Materials and Structures: Proceedings of CFRAC 2013*, 2013, p. 180.
- [34] H. Amor, J.-J. Marigo, C. Maurini, Regularized formulation of the variational brittle fracture with unilateral contact: Numerical experiments, *Journal of the Mechanics and Physics of Solids* 57 (2009) 1209–1229.
- [35] C. Miehe, M. Hofacker, F. Welschinger, A phase field model for rate-independent crack propagation: Robust algorithmic implementation based on operator splits, *Computer Methods in Applied Mechanics and Engineering* 199 (45–48) (2010) 2765–2778.

- 555 [36] F. Javadpour, D. Fisher, M. Unsworth, Nanoscale gas flow in shale gas sediments, *Journal of Canadian Petroleum Technology* 46 (10).
- [37] F. Javadpour, Nanopores and apparent permeability of gas flow in mudrocks (shales and siltstone), *Journal of Canadian Petroleum Technology* 48 (8) (2009) 16–21.
- 560 [38] S. A. Hosseini, F. Javadpour, G. E. Michael, Novel analytical core-sample analysis indicates higher gas content in shale-gas reservoirs, *SPE Journal* 20 (6) (2015) 1–397.
- [39] F. Civan, Effective correlation of apparent gas permeability in tight porous media, *Transport in Porous Media* 82 (2) (2010) 375–384.
- 565 [40] U. Pillai, Y. Heider, B. Markert, A diffusive dynamic brittle fracture model for heterogeneous solids and porous materials with implementation using a user-element subroutine, *Computational Materials Science* 153 (2018) 36 – 47.
- 570 [41] W. Zhu, C. Wei, S. Li, J. Wei, M. Zhang, Numerical modeling on destress blasting in coal seam for enhancing gas drainage, *International Journal of Rock Mechanics and Mining Sciences* 59 (2013) 179 – 190.
- [42] B. Bourdin, G. A. Francfort, J. J. Marigo, The variational approach to fracture, *Journal of Elasticity* 91 (2008) 5–148.
- [43] A. Logg, G. N. Wells, J. Hake, *DOLFIN: A C++/Python Finite Element Library*, Springer Berlin Heidelberg, Berlin, Heidelberg, 2012.
- 575 [44] P. R. Amestoy, I. S. Duff, J.-Y. L'Excellent, J. Koster, MUMPS: A general purpose distributed memory sparse solver, in: *International Workshop on Applied Parallel Computing*, Springer, 2000, pp. 121–130.
- 580 [45] T. Munson, J. Sarich, S. Wild, S. Benson, L. McInnes, Toolkit for advanced optimization (TAO) users manual, Tech. rep., Technical Report No. ANL/MCS-TM-322-Revision 3.5 (Argonne National Laboratory, 2014) (2014).
- 585 [46] S. Balay, S. Abhyankar, M. F. Adams, J. Brown, P. Brune, K. Buschelman, L. Dalcin, V. Eijkhout, W. D. Gropp, D. Kaushik, M. G. Knepley, D. A. May, L. C. McInnes, R. T. Mills, T. Munson, K. Rupp, P. Sanan, B. F. Smith, S. Zampini, H. Zhang, H. Zhang, PETSc users manual, Tech. Rep. ANL-95/11 - Revision 3.9, Argonne National Laboratory (2018).
- [47] C. Bilgen, A. Kopaničáková, R. Krause, K. Weinberg, A phase-field approach to conchoidal fracture, *Meccanica* 53 (6) (2018) 1203–1219.
- 590 [48] Z. A. Wilson, C. M. Landis, Phase-field modeling of hydraulic fracture, *Journal of the Mechanics and Physics of Solids* 96 (2016) 264–290.

- [49] C. Chukwudozie, Application of the variational fracture model to hydraulic fracturing in poroelastic media, Ph.D. thesis, Louisiana State University (2016).
- 595 [50] E. Detournay, D. Garagash, The near-tip region of a fluid-driven fracture propagating in a permeable elastic solid, *Journal of Fluid Mechanics* 494 (2003) 1–32.
- [51] J. Hu, D. Garagash, Plane-strain propagation of a fluid-driven crack in a permeable rock with fracture toughness, *Journal of Engineering Mechanics* 136 (9) (2010) 1152–1166.
- 600 [52] C. Miehe, M. Hofacker, F. Welschinger, A phase field model for rate-independent crack propagation: Robust algorithmic implementation based on operator splits, *Computer Methods in Applied Mechanics and Engineering* 199 (45–48) (2010) 2765–2778.
- 605 [53] M. Ambati, T. Gerasimov, L. De Lorenzis, A review on phase-field models of brittle fracture and a new fast hybrid formulation, *Computational Mechanics* 55 (2) (2015) 383–405.
- 610 [54] C. Miehe, F. Welschinger, M. Hofacker, Thermodynamically consistent phase-field models of fracture: Variational principles and multi-field FE implementations, *International Journal for Numerical Methods in Engineering* 83 (10) (2010) 1273–1311.
- [55] E. Detournay, A.-D. Cheng, Poroelastic response of a borehole in a non-hydrostatic stress field, in: *International Journal of Rock Mechanics and Mining Sciences & Geomechanics Abstracts*, Vol. 25, Elsevier, 1988, pp. 171–182.
- 615 [56] Y. L. Lu, D. Elsworth, L. G. Wang, Microcrack-based coupled damage and flow modeling of fracturing evolution in permeable brittle rocks, *Computers and Geotechnics* 49 (2013) 226–244.
- [57] I. N. Sneddon, M. Lowengrub, *Crack Problems in the Classical Theory of Elasticity*, Wiley, New York, 1969.
- 620 [58] M. F. Wheeler, T. Wick, W. Wollner, An augmented-Lagrangian method for the phase-field approach for pressurized fractures, *Computer Methods in Applied Mechanics and Engineering* 271 (2014) 69–85.
- [59] M. K. Hubbert, D. G. Willis, *Mechanics of Hydraulic Fracturing*, AAPG Special Volumes, 1972.
- 625 [60] B. Haimson, C. Fairhurst, Initiation and extension of hydraulic fractures in rocks, *Society of Petroleum Engineers Journal* 7 (03) (1967) 310–318.
- [61] C. H. Yew, X. Weng, *Mechanics of Hydraulic Fracturing*, Gulf Professional Publishing, 2014.